

RELATIVE EFFECT OF DIFFERENT ALLOYING ELEMENTS ON THE PEARLITE GROWTH

A Thesis Submitted
In Partial Fulfilment of the Requirements
for the Degree of
MASTER OF TECHNOLOGY

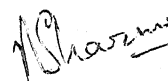
11152

By
SUDHIR KUMAR TEWARI

to the
DEPARTMENT OF METALLURGICAL ENGINEERING
INDIAN INSTITUTE OF TECHNOLOGY, KANPUR
MAY, 1984

CERTIFICATE

This is to certify that the work presented in this thesis entitled "Relative Effect of Different Alloying Elements on the Pearlite Growth" by Shri Sudhir Kumar Tewari has been carried out under my supervision and it has not been submitted elsewhere for a degree.



R.C. SHARMA

Assistant Professor

Department of Metallurgical Engineering
Indian Institute of Technology
Kanpur.

May, 1984

10 JUL 1984

LIT. SANPUH

CENTRAL LIBRARY

83415

Th

672.36

T 31 8

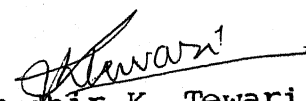
MME-1984-M-TEW-REL

ACKNOWLEDGEMENT

I take this opportunity to express my sincere gratitude to Dr. R.C. Sharma for his invaluable guidance and illuminating suggestions throughout the course of this work.

I would like to thank Mr. R.N. Srivastava for the excellent typing.

I am highly indebted to my friend Kulvir Singh for his help in the computer work. Finally, I am thankful to all my friends who made my stay here lively and flamboyant. Especially I am thankful to A. Verma, M.K. Maheshwari, D.K. Rawat, Doggie and P.K. Subramaniam who helped me when I was in need.


- Sudhir K. Tewari

CONTENTS

<u>Chapter</u>	<u>Page</u>
LIST OF FIGURES	vi
SYNOPSIS	viii
I. INTRODUCTION	1
II. LITERATURE REVIEW	3
II.1 Pearlite reaction in Fe-C system	3
II.1.a Volume Diffusion Model	5
II.1.b Boundary Diffusion Model	7
II.1.c Comparison between Theory and Experiments	9
II.2 Pearlite reaction in Fe-C-X system	9
II.2.a Para-Equilibrium	11
II.2.b Local-Equilibrium No-Partition	12
II.2.c Partitioning during the Pearlite Reaction	14
III. EFFECT OF ALLOYING ELEMENTS ON PEARLITE GROWTH	16
III.1 Introduction	16
III.2 Phase equilibria calculations	16
III.2.a Solution Models	16
(i) The Ferrite and Austenite Phases	16
(ii) The Cementite Phase	19
III.2.b Calculations for the Phase Equilibria	20
(i) True Equilibrium	20
(ii) Para-Equilibrium	21
(iii) Local-Equilibrium No-Partition	23
III.3 Pearlite growth rate calculations	24
III.3.a Low Supersaturation Partition Range	24
III.3.b High Supersaturation Region	28

IV.	RESULTS AND DISCUSSION	29
IV.1	Fe-C-Mn	29
IV.2	Fe-C-Cr	33
IV.3	Fe-C-Ni	34
IV.4	Fe-C-Si	35
V.	CONCLUSIONS	37
	REFERENCES	38
	APPENDIX (I)	
	APPENDIX (II)	
	APPENDIX (III)	
	APPENDIX (IV)	
	APPENDIX (V)	

LIST OF FIGURES

No.	Title
1.	Representation of the growth of lamellar pearlite by (i) volume diffusion and (ii) boundary diffusion
2.	Calculated binary Fe-C phase diagram
3.	Schematic representation of para-equilibrium in Fe-C-X system for (a) the $\gamma - \alpha$ and (b) the $\gamma - \text{cm}$ transformation
4.	Schematic representation of the local-equilibrium no-partition phase boundary in the Fe-C-X system for (a) the $\gamma - \alpha$ and (b) the $\gamma - \text{cm}$ transformation
5.	Schematic representation of the local-equilibrium no-partition phase boundaries in Fe-C-Mn alloys (after Gilmour)
6.	Schematic partition and no partition zones in the Fe-C-Cr system in the region of interest for the pearlite transformation (a) para-equilibrium and (b) local-equilibrium no-partition
7.	Schematic representation of the partitioning of alloying elements at low supersaturation range (Fe-C-Cr, Fe-C-Mn)
8.	Fe-C-Ni
9.	Fe-C-Si
10.	Calculated and experimental growth rates for 0.81 C steel
11.	Calculated para-equilibrium and local-equilibrium no-partition phase boundaries for 0.8 C-1.08 Mn alloy
12.	Calculated para-equilibrium and local-equilibrium no-partition growth rates for 0.69 C-1.8 Mn alloy
13.	Driving force for the phase boundary diffusion at low supersaturations
14.	Calculated and experimental growth rates for 0.8 C-1.08 Mn steel
15.	Calculated and experimental growth rates for 0.69 C-1.8 Mn steel

16. Calculated and experimental (after Razik et al.) partition data for steels at low supersaturations
17. Calculated para-equilibrium and local-equilibrium no-partition phase boundaries for 0.82 C-1.29 Cr alloy
18. Calculated para-equilibrium and local-equilibrium no-partition phase boundaries for 2.73% C-1.87% Cr alloy
19. Calculated and experimental growth rates for 0.82 C-1.92 Cr steel
20. Calculated and experimental growth rates for 2.73 C-1.87 Cr steel
21. Calculated para-equilibrium and local-equilibrium no-partition phase boundaries for 0.85 C-1.98 Ni alloy
22. Calculated para-equilibrium and local-equilibrium no-partition phase boundaries for 0.77 C-3.0 Ni alloy
23. Calculated and experimental growth rates for 0.85 C-1.98 Ni steel
24. Calculated and experimental growth rates for 0.77 C-3.0 Ni steel
25. Calculated and experimental growth rates for 0.84 C-1.99 Si steel.

SYNOPSIS

The pearlite growth rates for Fe-C-X alloys containing Mn, Cr, Ni and Si have been calculated on the basis of the theories evolved for the growth of pearlite in ternary systems. For this purpose, the phase equilibria have been calculated using the thermodynamic parameters available in literature. The calculated growth rates under para-equilibrium, local-equilibrium no-partition and partitioning conditions have been compared with the experimentally observed results.

In the low supersaturation range, the agreement between the calculated, alloying element, phase boundary diffusion controlled growth rates and experimentally measured values is good. In the high supersaturation range, at temperatures below L-E N-P Ae_1 , the experimental growth rates agree reasonably well with the local-equilibrium no-partition mechanism, which at still lower temperatures tend to shift towards the para-equilibrium mechanism.

The relative effect of these alloying elements on the pearlite growth (retardation of the growth rates) in the increasing order is Ni, Si, Mn and Cr.

CHAPTER I

INTRODUCTION

A large proportion of the steels used for machine parts can be classified as medium carbon, low alloy hardenability steels. The most significant parameter in defining the hardenability of steels is the critical cooling rate. To obtain 100% martensite a steel must be cooled at a rate faster than the critical cooling rate. At lower cooling rates, austenite decomposes into stable ferrite and pearlite, pearlite being the eutectoid product of austenite decomposition. Therefore, the kinetics of austenite decomposition is very important in determining the hardenability of the steels.

Understanding the mechanism through which alloying elements influence the kinetics of the decomposition of austenite is an important problem. All the common alloying elements (cobalt is an exception) retard the pearlite growth rate thus improve the hardenability of the steels. The effect of alloying elements in reducing the pearlite growth rate is not too well understood. There is, however, some consensus that for pearlite growth in Fe-C-X systems, two regions of different retardation mechanisms exist. At low supersaturations, the alloying element must partition between the ferrite and cementite phases and the growth is controlled by the diffusion of the alloying element through the phase boundary. At high supersaturations, however, the alloying element does not partition and the reaction is controlled by carbon diffusion

and the thermodynamic effect of the alloying element on the effective driving force for the diffusion of carbon. The relative importance of these mechanisms will vary with the alloying element and its concentration.

The no-partition reaction at high supersaturations can take place by two mechanisms, viz. local-equilibrium no-partition and para-equilibrium. In local-equilibrium no-partition reaction, ferrite and cementite of substantially the same alloying composition as the original austenite phase form, while still maintaining complete chemical equilibrium at the interface. In para-equilibrium the slow diffusing substitutional alloying element is unable to redistribute and thus the transformation proceeds under pure carbon diffusion control, precipitating the ferrite and cementite of same alloying element content as the austenite.

Evidence to the fact that these two mechanisms are involved in the growth of pearlite in Fe-C-X systems is available in literature. Experimental observations have been carried out on the pearlite growth in various Fe-C-X systems and partitioning of the alloying elements have been noticed. The present work was undertaken to determine the applicability of the established theories of pearlite growth in the Fe-C-X systems, containing manganese, chromium, nickel and silicon as alloy additions. Detailed and accurate thermodynamic and kinetic calculations were performed for these systems to verify the existing theories.

CHAPTER II

LITERATURE REVIEW

II.1 Pearlite reaction in Fe-C system

The binary Fe-C system has long been the subject of intensive study (1-3). In the eutectoid (or pearlite) reaction the high temperature austenite phase transforms to a lamellar structure consisting of parallel lamellae of ferrite and cementite (Fe_3C). It is a first order transformation and occurs by nucleation and growth. As in almost all other cases, nucleation occurs heterogeneously and not homogeneously. If the austenite is homogeneous, nucleation occurs almost exclusively at grain boundaries, otherwise it can occur heterogeneously as well as homogeneously (4). Mehl (5) has suggested that pearlite develops by nucleation of cementite, however, Hillert (6) and Sharma and Purdy (7) have recently suggested that pearlite grows by the nucleation of ferrite.

For plain carbon and simple alloy steels the radial growth velocity of a pearlite colony is often constant for a given temperature of transformation, although the isothermal nucleation rate of new colonies increases rapidly with time. At high rates of nucleation all the available sites for nucleation may be used up early in the reaction. This kinetic behaviour is called site saturation, and once it has occurred the reaction is entirely controlled by growth. If site saturation occurs early in reaction, which is true for the transformation temperatures in the vicinity of the nose of

the TTT diagram, then transformation will be complete in the time required for pearlite to grow to the centres of austenite grains. All alloy additions which improve hardenability by reducing the overall reaction rate do so primarily by influencing the pearlite growth rate instead of nucleation rate, this is particularly true for transformation temperatures up to 100°C above the nose of the TTT diagram (48). The nucleation problem will not be discussed further in the present work.

In a binary or a ternary system the diffusional analysis of pearlite growth is complicated by the fact that there exist two possible diffusion paths for the redistribution of the solute(s) to the product phases. In Fe-C system, carbon has the options of moving by volume diffusion through the bulk austenite or by boundary diffusion along the austenite/ferrite and austenite/cementite interfaces. An elementary theory of pearlite growth was first proposed by Zener (8). Zener described the problem of pearlite growth by volume diffusion of carbon, this problem has been rigorously treated by subsequent workers (11-14). Following the disparity in the theoretical and experimental results, a number of workers have investigated the problem on the basis of the boundary diffusion of carbon and other mechanisms (9,10,15,16). Recently, Puls and Kirkaldy (17) have considered the variation in the carbon volume diffusion coefficient in austenite with concentration of carbon and have shown that the volume diffusion model satisfactorily describes

the pearlite growth data in Fe-C at higher temperatures. However, partial involvement of boundary diffusion of carbon at lower temperatures ($< 550^{\circ}\text{C}$) is also possible.

In the following sections the volume and boundary diffusion models of pearlite growth are briefly discussed.

II.1.a Volume Diffusion Model

Figure (2) shows the Fe-C phase diagram, the dashed line defines the region where pearlite reaction can take place. Figure (1) shows schematically the pearlite/austenite interface. Local equilibrium is assumed to exist across this interface. Pearlite grows by cooperative precipitation of lamellae, in such a case there exists a situation, at the junction of the two lamellae, where three phases must exist in local-equilibrium below the eutectoid temperature. This is achieved through the modification of phase diagram due to the capillarity. In this way the concentration across the junction can vary smoothly in the parent phase. To accommodate the equilibrium of the surface tension forces, at the three phase junction, the curvature of the interface is essential. The local radius of curvature generates a pressure which is assumed to act mainly on the product phases. This leads to a variation of composition along the interface, which is everywhere in local-equilibrium.

Zener (8) had suggested a simple theory accommodating all these considerations. Assuming austenite/ferrite and austenite/cementite interfaces to be flat, the concentration

difference which provide the driving force for diffusion would be $(C_C^{Y\alpha} - C_C^{Ycm})$, where $C_C^{Y\alpha}$ and C_C^{Ycm} are the equilibrium concentration according to the phase diagram for austenite in contact with ferrite and cementite, respectively. According to Zener the capillary modified difference can be approximately represented by $(1 - \frac{S}{S_0})(C_C^{Y\alpha} - C_C^{Ycm})$, where S is the interlamellar spacing and S_0 is the critical interlamellar spacing. S_0 is a function of temperature only. At the critical interlamellar spacing no concentration difference exists, the thermodynamic driving force for the pearlite reaction is exactly balanced by the interfacial energy stored in the ferrite/cementite interfaces and the pearlite growth velocity necessarily goes to zero.

Further, Zener supposed that effective distance for diffusion up to the edge of a cementite lamella is proportional to its thickness, so the flux

$$J = -D_C \frac{dC}{dx} \cong -D_C \frac{C_C^{Y\alpha} - C_C^{Ycm}}{a S^{cm}} \left(1 - \frac{S}{S_0}\right) \quad (II.1)$$

or from mass balance

$$J = -v (C_C^{cm} - C_C^{\alpha}) \quad (II.2)$$

where, v is the pearlite growth rate, D_C is the volume diffusion coefficient of carbon in austenite and C_C^{cm} and C_C^{α} are the concentrations of the cementite and the ferrite, respectively. From the lever rule

$$S^\alpha (C_{C\infty}^\gamma - C_C^\alpha) = S^{cm} (C_C^{cm} - C_{C\infty}^\gamma) = \frac{S^{cm} S^\alpha}{S} (C_C^{cm} - C_C^\alpha) \quad (II.3)$$

So a combination of equations (II.1), (II.2) and (II.3) yields

$$v = \frac{D_C}{a} \frac{S^2}{S^\alpha S^{cm}} \cdot \frac{(C_C^{\gamma\alpha} - C_C^{\gamma cm})}{(C_C^{cm} - C_C^\alpha)} \cdot \frac{1}{S} \left(1 - \frac{S_0}{S}\right) \quad (II.4)$$

Brandt (12) and Scheil (13) were the first to construct a comprehensive volume diffusion model for the pearlite transformation. A more rigorous calculation has been performed by Hillert (14). Bolze et al. (11) generalised Hillert's volume diffusion model to take into account the non-uniformity of concentration in the product phases, which results from a variation of curvature along the pearlite/austenite interface. The Bolze et al. and Hillert treatments are not discussed here.

II.1.b Boundary Diffusion Model

The boundary diffusion model for lamellar growth was first applied to the problem of discontinuous precipitation by Turnbull (9) and by Chan (10). Various attempts to determine boundary diffusion controlled eutectoid reaction have since been made. The carbon is assumed to diffuse through a pearlite/austenite interface of thickness δ and diffusion coefficient D_B . To a first approximation the growth equation for pearlite can be obtained from the volume diffusion model by substituting a boundary diffusion

coefficient, D_B , for the volume diffusion coefficient, D_C , and decreasing the "window" for volume diffusion $1/S$ by the ratio δ/S . This leads to

$$v \propto \frac{D_B \delta}{S^2} \left(1 - \frac{S_0}{S}\right) \quad (\text{II.5})$$

A more detailed solution for the boundary diffusion model has been obtained by Hillert (14) and by Shapiro and Kirkaldy (15). Considering the mass balance in a thin strip of material parallel to the ferrite/cementite interface (Figure 1), Hillert obtained the following velocity equation

$$v = 12 K D_B \delta \cdot \frac{S^2}{S^\alpha S^{\text{cm}}} \cdot \frac{(C_C^{\gamma\alpha} - C_C^{\gamma\text{cm}})}{(C_C^{\text{cm}} - C_C^\alpha)} \cdot \frac{1}{S^2} \left(1 - \frac{S_0}{S}\right) \quad (\text{II.6})$$

Shapiro and Kirkaldy, following a more rigorous but less general argument obtained for a symmetric eutectoid

$$v = 24 \delta D_B \frac{(C_C^{\gamma\alpha} - C_C^{\gamma\text{cm}})}{1/2 - a} \cdot \frac{1}{S^2} \left(1 - \frac{S_0}{S}\right) \quad (\text{II.7})$$

where

$$D_B = 2 q V L \quad (\text{II.8})$$

q and a are equilibrium thermodynamic parameters obtained from the free energy-composition diagram, V is the molar volume and L is the Onsager phenomenological coefficient (mobility) for boundary diffusion. Lack of the knowledge of the D_B restricts the quantitative measurement of this model.

II.1.c Comparison between Theory and Experiments

Early comparison between the experimental pearlite growth rates in Fe-C alloys and the volume diffusion theory were unsuccessful. Following this, some of the investigators suggested that major proportion of carbon diffusion takes place through the boundary layer separating the pearlite and the austenite. However, Brown and Ridley (19), assuming volume diffusion control, back-calculated the effective carbon diffusivity in austenite from the pearlite growth data and found D_C values only 2 to 4 times higher than the experimental diffusion coefficients. They also found that for small under-coolings the effective D_C almost remains constant with decreasing temperature. Kirkaldy and Puls (17, 18) attributed this to the fact that the diffusion coefficient of carbon in austenite is strongly concentration dependent. Puls and Kirkaldy recalculated the pearlite growth rate using Hillert's volume diffusion model, taking into account the variation in D_C with concentration, and found that this model agrees with the experimental results within a factor of 2. At temperatures lower than about 550°C, the partial involvement of boundary diffusion is also possible.

II.2 Pearlite reaction in Fe-C-X system

The effect of alloying elements during the austenite decomposition reactions has been theoretically and experimentally investigated by many workers. In Fe-C-X system, where X is a substitutional alloying element, carbon diffuses

much faster than alloying elements. In such a case the volume diffusion controlled austenite decomposition to pearlite can take place in two ways. In the first case, the alloying element is partitioned between the product phases (ferrite and cementite). Such a reaction is called partitioning reaction. In this case the reaction rate is slowed down considerably due to the relatively slow diffusion of the alloying element. In the second case, the alloying element undergoes no long range diffusion and the ratio of the alloying element to iron remains the same in both the product phases as in the parent phase. The reaction in this case is controlled by carbon diffusion. An alloying element affects the reaction kinetics only through its thermodynamic influence on the driving force for the reaction. Such a reaction is called no-partition reaction. In general, the partitioning reaction must take place at low supersaturations while the no-partitioning reaction can take place at high supersaturations. The actual temperature of partition - no-partition transition - if it exists, would depend on the alloy system and composition.

Partitioning during the pro-eutectoid ferrite formation has been widely reported in the literature. Experimentally, the study of partitioning during the pearlite reaction is much more difficult. Nonetheless, quite a few attempts have been made to study partitioning during the pearlite reaction. Bowman (20) observed partitioning of molybdenum between ferrite and cementite in the pearlite formed in

Fe-C-Mo alloys down to 600°C. Picklesimer et al. (21) observed that the manganese partitions between ferrite and cementite during the pearlite reaction in Fe-C-Mn alloys at low supersaturations but not at high supersaturations. They were unable to determine the partition-no-partition transition temperature accurately. Recently, Razik et al. (22,23) have studied the partitioning of manganese and chromium. In both the cases they observed partitioning at low supersaturations and non-partitioning at high supersaturations. Similar studies for chromium have been carried out by Chance and Ridley (47). These appear to be the most reliable results reported so far in this context.

For the temperature and composition range of interest with respect to pearlite growth, the general features of a ternary isotherm corresponding to a particular Fe-C-X system are dependent on whether X is a ferrite or an austenite stabiliser and whether it is a carbide former or not. The various possibilities can be conveniently grouped in two categories which depend on whether X depresses (e.g. Mn and Ni) or raises (e.g. Cr and Si) the eutectoid temperature (17).

The partitioning and no-partitioning regions of the Fe-C-X phase diagram are briefly discussed in the following sections.

II.2.a Para-Equilibrium

One way in which a no-partition reaction can take place is para-equilibrium. In this case there is no

partitioning of alloying element X, and the growth rate is controlled by diffusion of carbon. Hillert (24) and Rudberg (25) have discussed the position of the para-equilibrium phase boundaries in ternary Fe-C-X alloy systems. Hillert (14) has shown that the para-equilibrium phase boundaries can be calculated from a knowledge of the free energy surfaces. A true para-equilibrium tie-line must satisfy the criterion that the chemical potential of the fast diffusing element (carbon) must be the same in both the phases (austenite and ferrite or cementite). While the ratio of the alloying element to iron remains constant in both the phases ($x_X^\alpha/x_{Fe}^\alpha = x_X^{cm}/x_{Fe}^{cm} = x_X^Y/x_{Fe}^Y$). The para-equilibrium phase boundaries must lie within the thermodynamically stable two phase field. Gilmour et al. (26) and Sharma and Kirkaldy (27) and Sharma et al. (28) have calculated such para-equilibrium phase boundaries for Fe-C-Mn, Fe-C-Ni and Fe-C-Cr systems from basic thermodynamic data. A schematic representation of such boundaries is shown in Figure (3).

II.2.b Local-Equilibrium No-Partition

Another way in which no-partition reaction can take place is called the local-equilibrium no-partition condition. This has been described by Kirkaldy (29), Hillert (14), Coates (30,31) and others. Under this condition the precipitating phase, during a diffusion controlled austenite decomposition in Fe-C-X system, may have substantially the same alloying element composition and still maintain a

complete local-equilibrium at the interface. Kirkaldy (29) and Purdy (32) established, after finding solutions for the transformation assuming local-equilibrium at the interface and extending these to the Fe-C-Mn system, that at low supersaturations these solutions predict manganese partition and low growth rates due to manganese diffusion control, while at higher supersaturations the manganese need not partition and the transformation would be controlled by carbon diffusion. The position of this local-equilibrium partition-no-partition boundary in the ternary Fe-C-X phase diagram has been further considered by Hillert (14), Coates (30,31) and others. The construction of such boundary is schematically shown in Figure (4). The intersection of the carbon component ray ($\frac{X_X}{X_{Fe}} = \text{Constant}$ line) from the ferrite or cementite end of a tie-line in the stable $\alpha + \gamma$ or $\gamma + \text{cm}$ two phase field and the extrapolation of the carbon iso-activity line in austenite from austenite end of the tie-line define a point on the partition-no-partition boundary. The locus of such points divides the two phase ($\alpha + \gamma$ or $\gamma + \text{cm}$) region into partition and no-partition regions.

In the high supersaturation region the two no-partition conditions described above could exist. At high supersaturations, at early stages of reaction or high reaction rates, para-equilibrium mechanism appears to be operating which at later stages of the transformation may change to local-equilibrium mechanism. Figure (5) (after Gilmour)

schematically shows the possible regions in a Fe-C-X isotherm and the mechanisms which may be in operation.

II.2.c Partitioning during the Pearlite Reaction

In the preceding section of this chapter the para-equilibrium and local-equilibrium no-partition boundaries for the precipitation of ferrite and cementite have been discussed. Figure (6) schematically shows the general regions of partition, no-partition reactions in the Fe-C-Cr system in the range where the pearlite reaction is feasible. The theory discussed here is applicable to other systems also. The para-equilibrium or local-equilibrium no-partition eutectoid point on such a diagram can easily be defined, as shown in the Figure (6).

In region C of Figure (6) partitioning of X is thermodynamically required for the precipitation of ferrite as well as cementite, so the same is true for the reaction $\gamma = \alpha + \text{cm}$. In region A, ferrite and cementite can both precipitate without partitioning and hence the pearlite reaction can thermodynamically proceed without the partitioning of X. In the region B only one of the two phases (ferrite or cementite) requires the partitioning of the alloying element. There are two possibilities in this case. Since the kinetics of the no-partition reaction is much faster than the partitioning reaction, the phase which requires no partitioning can precipitate first and grow until the matrix composition shifts into region A or C and then the pearlite reaction can

proceed accordingly. The other possibility is that the capillarity effects during the pearlite reaction modify the phase diagram in such a way that the alloy falls in region A or C and the pearlite reaction again takes place accordingly. In either case a carbon component ray ($X_X/X_{Fe} = \text{Constant}$) passing through the no-partition eutectoid point would divide the pearlite reaction region into regions where partitioning is required and where no partitioning is thermodynamically feasible. Since, generally, in practice no primary ferrite or cementite is observed in alloys in the B region, the second possibility seems to be operative.

CHAPTER III

EFFECT OF ALLOYING ELEMENTS ON PEARLITE GROWTH

III.1 Introduction

A detailed calculations were carried out for the pearlite growth rate in different Fe-C-X systems, based on the theory discussed in the previous chapter. Four alloying elements Mn, Cr, Ni and Si have been considered. The results of such theoretical calculations were compared with the available experimental results to verify the validity of the existing pearlite growth theories.

Equilibria involving austenite, ferrite and cementite in Fe-C system have been analysed by Harvig (33). A comprehensive study of the Fe-C-X systems, involving Cr, Mn, Ni and Si as alloy additions has been done by Urhenius (34). The phase boundaries, under the conditions of complete equilibrium, para-equilibrium and local-equilibrium no-partition relevant for the pearlite growth calculations, are calculated by using the thermodynamic data given by Urhenius (34) and briefly described below.

III.2 Phase equilibria calculations

III.2.a Solution Models

(i) The Ferrite and Austenite Phases: For the ferrite and the austenite, the solutions containing substitutional as well as interstitial solute, a simplified version of the model

suggested by Hillert and Staffansson (35) has been adopted. This assumes a four component solution with substitutional mixing of iron and alloying element on a cubic lattice and carbon and vacancies mixing on the corresponding interstitial sublattice. For such a model the molar ratios Y_i are defined as

$$Y_{Fe} = \frac{X_{Fe}}{1 - X_C} \quad (III.1)$$

$$Y_M = \frac{X_M}{1 - X_C} \quad (III.2)$$

$$Y_C = \frac{a}{c} \cdot \frac{X_C}{1 - X_C} \quad (III.3)$$

subject to mass conservation condition

$$X_{Fe} + X_M + X_C = 1 \quad (III.4)$$

$$\text{and } Y_{Fe} + Y_M = 1 \quad (III.5)$$

where, M and C stand for substitutional alloying element and carbon, respectively. X_i represents the mole fractions of the elements involved. In equation (III.3), $\frac{c}{a}$ is the number of interstitial sites per lattice site, for austenite $c = a = 1$ and for ferrite $a = 1$ and $c = 3$. From the expression for the Gibbs energy as given by Hillert and Staffansson (35) the following partial quantities are obtained

$$\bar{G}_{Fe} = {}^0G_{Fe} + RT \ln Y_{Fe} + \frac{c}{a} RT \ln (1 - Y_C) + E_{G_{Fe}} \quad (III.6)$$

$$\bar{G}_M = {}^0G_M + RT \ln Y_M + \frac{c}{a} RT \ln (1 - Y_C) + E_{G_M} \quad (III.7)$$

$$\bar{G}_C = {}^oG_C + RT \ln \left(\frac{Y_C}{1 - Y_C} \right) + E_{G_C} \quad (\text{III.8})$$

where, \bar{G}_i stands for partial molar free energy, T is temperature in degrees Kelvin, oG_i is standard free energy and E_{G_i} represents excess free energy of mixing. The excess free energies are given as follows

$$\begin{aligned} a \ E_{G_{Fe}} = & - Y_M Y_C (\Delta G_M + {}^oL_{FeM}^C - {}^oL_{FeM}^V + L_{Cv}^M - L_{Cv}^{Fe} \\ & + (1 - 2Y_M)({}^1L_{FeM}^V - {}^1L_{FeM}^C)) + Y_M^2({}^oL_{FeM}^V \\ & + (3 - 4Y_M) {}^1L_{FeM}^V) + Y_C^2 L_{Cv}^{Fe} + 2Y_M Y_C ({}^oL_{FeM}^C - {}^oL_{FeM}^V \\ & + (2 - 3Y_M)({}^1L_{FeM}^C - {}^1L_{FeM}^V)) + 2Y_M Y_C^2 (L_{Cv}^M - L_{Cv}^{Fe}) \end{aligned} \quad (\text{III.9})$$

$$\begin{aligned} a \ E_{G_M} = & Y_{Fe} Y_C (\Delta G_M + {}^oL_{FeM}^V - {}^oL_{FeM}^C + L_{Cv}^M - L_{Cv}^{Fe} \\ & + (1 - 2Y_M)({}^1L_{FeM}^V - {}^1L_{FeM}^C)) + Y_{Fe}^2({}^oL_{FeM}^V + \\ & + (1 - 4Y_M) {}^1L_{FeM}^V) + Y_C^2 L_{Cv}^M + 2Y_{Fe}^2 Y_C ({}^oL_{FeM}^C - {}^oL_{FeM}^V \\ & + (1 - 3Y_M)({}^1L_{FeM}^C - {}^1L_{FeM}^V)) + 2Y_{Fe} Y_C^2 (L_{Cv}^{Fe} - L_{Cv}^M) \end{aligned} \quad (\text{III.10})$$

$$\begin{aligned} c \ E_{G_C} = & - 2Y_C L_{Cv}^{Fe} + Y_M (\Delta G_M + {}^oL_{FeM}^C - {}^oL_{FeM}^V + L_{Cv}^M - L_{Cv}^{Fe}) \\ & + 2Y_M Y_C (L_{Cv}^{Fe} - L_{Cv}^M) + Y_M^2 ({}^oL_{FeM}^V - {}^oL_{FeM}^C) \end{aligned} \quad (\text{III.11})$$

where, G_M and L 's are the solution model parameters.

(ii) The Cementite Phase: The Gibbs energy of cementite is described by a thermodynamic model originally developed by Richardson (36) and by Hillert et al. (37) for carbides. The carbide formula M_3C is written as $MC_{1/3}$, because all the thermodynamic quantities in the following equations are referred to one mole of metal atoms. The ternary cementite $(FeM)C_{1/3}$ is considered as a solid solution of $FeC_{1/3}$ and $MC_{1/3}$ where Fe and M randomly mix on the metal sublattice and the carbon sublattice is fixed. Under these conditions the free energy of mixing of $(FeM)C_{1/3}$ can be written as

$$\Delta G_{(FeM)C_{1/3}} = Y_{Fe} \bar{G}_{FeC_{1/3}}^{cm} + Y_M \bar{G}_{MC_{1/3}}^{cm} \quad (III.12)$$

The following equations express the partial Gibbs energy of the cementite

$$\bar{G}_{FeC_{1/3}}^{cm} = {}^o G_{FeC_{1/3}}^{cm} + RT \ln Y_{Fe}^{cm} + A_{FeM}^{cm} (Y_M^{cm})^2 \quad (III.13)$$

$$\bar{G}_{MC_{1/3}}^{cm} = {}^o G_{MC_{1/3}}^{cm} + RT \ln Y_M^{cm} + A_{FeM}^{cm} (Y_{Fe}^{cm})^2 \quad (III.14)$$

where molar concentrations Y_i are given by

$$Y_M^{cm} = \frac{X_M^{cm}}{X_M^{cm} + X_{Fe}^{cm}} \quad (III.15)$$

$$Y_{Fe}^{cm} = \frac{X_{Fe}^{cm}}{X_M^{cm} + X_{Fe}^{cm}} \quad (III.16)$$

The parameter A_{FeM}^{cm} represents the interaction between iron and the alloying element in the cementite and ${}^{\circ}G_{FeC_{1/3}}^{cm}$ and ${}^{\circ}G_{MC_{1/3}}^{cm}$ are standard free energies of formation.

III.2.b Calculations for the Phase Equilibria

(i) True Equilibrium: The phase equilibrium between ferrite and austenite is obtained by equating the partial molar free energies of each component in the two phases, i.e.,

$$\bar{G}_i^{\alpha} = \bar{G}_i^{\gamma} \quad (i = Fe, C, M) \quad (III.17a,b,c)$$

Substituting equations (III.6), (III.7) and (III.8) into (III.17) we obtain

$$\frac{Y_{Fe}^{\gamma}(1 - Y_C^{\gamma})}{Y_{Fe}^{\alpha}(1 - Y_C^{\alpha})^3} = \exp \frac{1}{RT} ({}^{\circ}G_{Fe}^{\alpha} - {}^{\circ}G_{Fe}^{\gamma} + E_{Fe}^{\alpha} - E_{Fe}^{\gamma}) \quad (III.18a)$$

$$\frac{Y_M^{\gamma}(1 - Y_C^{\gamma})}{Y_M^{\alpha}(1 - Y_C^{\alpha})^3} = \exp \frac{1}{RT} ({}^{\circ}G_M^{\alpha} - {}^{\circ}G_M^{\gamma} + E_M^{\alpha} - E_M^{\gamma}) \quad (III.18b)$$

and

$$\frac{Y_C^{\gamma}(1 - Y_C^{\alpha})}{Y_C^{\alpha}(1 - Y_C^{\gamma})} = \exp \frac{1}{RT} ({}^{\circ}G_C^{\alpha} - {}^{\circ}G_C^{\gamma} + E_C^{\alpha} - E_C^{\gamma}) \quad (III.18c)$$

These are equations involving four independent concentration terms. By fixing temperature and the value of one concentration term, equations (III.18) can be solved for other three concentrations, thus define a single tie-line in the $\alpha + \gamma$ field.

The austenite-cementite equilibrium is given by

$$\bar{G}_{MC}^Y_{1/3} + \frac{1}{3} \bar{G}_C^Y = \bar{G}_{MC}^Y_{1/3} \quad (\text{III.19a,b})$$

where M stands for iron and the alloying element. Substituting equations (III.13) and (III.14) into equations (III.19) and rearranging

$$\begin{aligned} \frac{Y_{Fe}^{cm}/Y_{Fe}^{cm}}{Y_M^Y/Y_{Fe}^Y} &= \exp \frac{1}{RT} ({}^oG_{FeC}^{cm}_{1/3} - {}^oG_{MC}^{cm}_{1/3} + {}^oG_M^Y - {}^oG_{Fe}^Y \\ &+ E_{G_M}^Y - E_{G_{Fe}}^Y + A_{FeM}^{cm}(1 - 2Y_{Fe}^{cm}) \end{aligned} \quad (\text{III.20a})$$

$$\begin{aligned} \frac{Y_{Fe}^Y}{Y_{Fe}^{cm}} (Y_C^Y)^{1/3} (1 - Y_C^Y)^{2/3} &= \exp \frac{1}{RT} ({}^oG_{FeC}^{cm}_{1/3} - {}^oG_{Fe}^Y - \frac{1}{3} {}^oG_C^Y \\ &+ A_{FeM}^{cm}(Y_M^{cm})^2 - \frac{1}{3} E_{G_C}^Y - E_{G_{Fe}}^Y) \end{aligned} \quad (\text{III.20b})$$

In this case there are only two equations involving three independent concentrations; two for the austenite phase and only one for cementite, since the carbon concentration in cementite is fixed. By fixing one concentration the other two can be solved by computer iterations.

(ii) Para-Equilibrium: The thermodynamic conditions defining para-equilibrium for austenite to ferrite transformation, as discussed in the earlier chapter, are given by

$$\bar{G}_C^\alpha = \bar{G}_C^Y \quad (\text{III.21})$$

$$X_{Fe}^\alpha \bar{G}_{Fe}^\alpha + X_M^\alpha \bar{G}_M^\alpha = X_{Fe}^Y \bar{G}_{Fe}^Y + X_M^Y \bar{G}_M^Y \quad (\text{III.22})$$

and

$$\frac{X_{Fe}^{\alpha}}{X_M^{\alpha}} = \frac{X_{Fe}^{\gamma}}{X_M^{\gamma}} = \frac{X_{Fe}}{X_M} = \text{Constant} \quad (\text{III.23})$$

By substituting the partial molar quantities in the above equations, we get

$$\frac{Y_C^{\gamma}(1 - Y_C^{\alpha})}{Y_C^{\alpha}(1 - Y_C^{\gamma})} = \exp \frac{1}{RT} (^{\circ}G_C^{\alpha} - ^{\circ}G_C^{\gamma} + E_{G_C}^{\alpha} - E_{G_C}^{\gamma}) \quad (\text{III.24a})$$

$$\begin{aligned} \frac{(1 - Y_C^{\gamma})}{(1 - Y_C^{\alpha})^3} &= \exp \frac{1}{RT} (Y_{Fe} (^{\circ}G_{Fe}^{\alpha} - ^{\circ}G_{Fe}^{\gamma}) + Y_M (^{\circ}G_M^{\alpha} - ^{\circ}G_M^{\gamma}) \\ &\quad + Y_{Fe} (E_{G_{Fe}}^{\alpha} - E_{G_{Fe}}^{\gamma}) + Y_M (E_{G_M}^{\alpha} - E_{G_M}^{\gamma})) \end{aligned} \quad (\text{III.24b})$$

and

$$\frac{Y_{Fe}^{\alpha}}{Y_M^{\alpha}} = \frac{Y_{Fe}^{\gamma}}{Y_M^{\gamma}} = \frac{Y_{Fe}}{Y_M} = \text{Constant} \quad (\text{III.24c})$$

Equations (III.24) are solved for a number of given $\frac{Y_M}{Y_{Fe}}$ ratios to give the para-equilibrium two phase field, $\alpha + \gamma$, for a given temperature by computer iterations.

For austenite to cementite transformation the thermodynamic conditions defining the para-equilibrium are

$$Y_{Fe} \bar{G}_{Fe}^{\gamma} + Y_M \bar{G}_M^{\gamma} + \frac{1}{3} \bar{G}_C^{\gamma} = \Delta G_{(FeM)C}^{\gamma} / 3$$

or more precisely,

$$Y_{Fe} \bar{G}_{Fe}^{\gamma} + Y_M \bar{G}_M^{\gamma} + \frac{1}{3} \bar{G}_C^{\gamma} = Y_{Fe} \bar{G}_{FeC}^{cm} / 3 + Y_M \bar{G}_{MC}^{cm} / 3 \quad (\text{III.25})$$

and

$$\frac{X_{Fe}^{\gamma}}{X_M^{\gamma}} = \frac{X_{Fe}^{cm}}{X_M^{cm}} = \text{Constant} \quad (\text{III.26})$$

Substituting partial molar quantities in the above equations, we get,

$$\begin{aligned}
 (Y_C^\gamma)^{1/3} (1 - Y_C^\gamma)^{2/3} &= \exp \frac{1}{RT} (Y_{Fe} ({}^oG_{FeC}^{cm})_{1/3} - {}^oG_{Fe}^\gamma - \frac{1}{3} {}^oG_C^\gamma) \\
 &+ Y_M ({}^oG_{MC}^{cm})_{1/3} - {}^oG_M^\gamma - \frac{1}{3} {}^oG_C^\gamma) - Y_{Fe} E_{Fe}^\gamma - Y_M E_M^\gamma \\
 &- \frac{1}{3} E_C^\gamma + Y_M Y_{Fe} A_{FeM}^{cm} \quad (III.27a)
 \end{aligned}$$

and

$$\frac{Y_{Fe}^\gamma}{Y_M^\gamma} = \frac{Y_{Fe}^{cm}}{Y_M^{cm}} = \frac{Y_{Fe}}{Y_M} = \text{Constant} \quad (III.27b)$$

Equation (III.27a) solved for Y_C for a series of given values of Y_{Fe}/Y_M generates a para-equilibrium $\gamma/(\gamma + cm)$ phase boundary.

(iii) Local-Equilibrium No-Partition: The local-equilibrium no-partition boundary is calculated from the intersection of the iso-activity line of carbon in austenite from the austenite end of the tie-line and the carbon component ray ($\frac{X_{Fe}}{X_M} = \text{Constant}$) from the ferrite or cementite end of the tie-line, as shown in Figure (4). The local-equilibrium no-partition boundary conditions can be written as follows

$$\frac{Y_C^{\gamma L} (1 - Y_C^\gamma)}{Y_C^\gamma (1 - Y_C^{\gamma L})} = \exp \frac{1}{RT} (E_C^\gamma - E_C^{\gamma L}) \quad (III.28a)$$

and

$$\frac{Y_M^{\gamma L}}{Y_{Fe}^{\gamma L}} = \frac{Y_M^{\alpha}}{Y_{Fe}^{\alpha}} \quad \text{for } \alpha - \gamma \text{ equilibrium} \quad (\text{III.28b})$$

or

$$\frac{Y_M^{\gamma L}}{Y_{Fe}^{\gamma L}} = \frac{Y_M^{\gamma cm}}{Y_{Fe}^{\gamma cm}} \quad \text{for } \gamma - \text{cm equilibrium} \quad (\text{III.28c})$$

where, $Y_M^{\gamma L}$, $Y_C^{\gamma L}$ and $Y_{Fe}^{\gamma L}$ are the local-equilibrium no-partition boundary concentrations and Y_M^{α} , Y_{Fe}^{α} , Y_M^{γ} , Y_{Fe}^{γ} and Y_C^{γ} are the equilibrium tie-line concentrations in the $(\alpha + \gamma)$ field. Once the equilibrium tie-lines are known, equations (III.28) can be readily solved for the local-equilibrium no-partition boundary.

For all the above calculations the value of the thermodynamic parameters have been taken from the references (33), (34), (38) and (39). These values are tabulated in Appendix (I). The computer programmes for the calculation of ferrite-austenite and austenite-cementite are given in Appendices (II) and (III), respectively.

III.3 Pearlite growth rate calculations

III.3.a Low Supersaturation Partition Range:

As discussed in the previous chapter, in the temperature range where the partitioning of the alloying element takes place, the pearlite growth rate is controlled by the diffusion of alloying element through the pearlite/austenite interface. The pearlite growth velocity in this case is given by equation (III.6), i.e.

$$v = 12 K D_B \delta \frac{S^2}{S^\alpha S^{cm}} \cdot \frac{(C_M^{\gamma\alpha} - C_M^{\gamma cm})}{\bar{C}_M} \cdot \frac{1}{S^2} \left(1 - \frac{S_0}{S}\right) \quad (\text{III.29})$$

Taking $\frac{S^{cm}}{S} = \frac{1}{8}$ and $\frac{S^\alpha}{S} = \frac{7}{8}$, and $S = 2S_0$ (43) equation (III.29) becomes

$$v = 54 K D_B \delta \left(\frac{C_M^{\gamma\alpha} - C_M^{\gamma cm}}{\bar{C}_M} \right) \frac{1}{S^2} \quad (\text{III.30})$$

where, \bar{C}_M is the concentration of alloying element in the alloy in weight percent. All other terms have been defined earlier. The value of $K D_B \delta$ was calculated using the equation developed by Fridberg et al. (44), viz.

$$K \delta D_B = 5.4 \times 10^{-8} \exp\left(\frac{-154,808 \text{ J/mole}}{RT}\right) \text{ cm}^3/\text{sec} \quad (\text{III.31})$$

Equations (III.30) and (III.31) were used to calculate the growth rate at low supersaturations.

Assuming a uniform carbon activity in austenite in front on the pearlite-austenite interface, the driving force for the alloying element boundary diffusion-controlled growth can be calculated. The calculations for the driving force, for the diffusion of alloying through the austenite/pearlite interface, for different systems are briefly discussed below.

Fe-C-Mn and Fe-C-Cr Systems: Assuming local equilibrium at the interface and a steady state pearlite growth, the interface composition for a flat interface condition and consistent with the theory discussed in the Section II.2.c can be obtained by the construction shown in Figure (7).

In Figure (7), which shows, schematically, the phase boundaries for Fe-C-Mn or Fe-C-Cr systems, point O is the original alloy composition, points a and d denote the compositions in ferrite and cementite, respectively. Lines ab and cd are the tie-lines describing the ferrite-austenite and austenite-cementite interface compositions, respectively, and the line going through b and c is the carbon iso-activity line ahead of the pearlite/austenite interface. The carbon iso-activity line, in general, may not go through point O. The difference is accommodated by capillarity effect. The driving force for the boundary diffusion will then be proportional to $(C_M^{Y^\alpha} - C_M^{Y^{cm}})$.

For calculating these concentrations, the thermodynamic equations defining the true equilibrium condition for ferrite-austenite equilibrium are solved for a given value of Y_M^α . Since line aod is a straight line and Y_{Fe}^{cm} and Y_M^{cm} are known, Y_M^{cm} can be calculated. For this value of Y_M^{cm} the tie-line describing the austenite-cementite phase boundary concentrations is calculated. Now for the calculated values of the concentrations, the partial molar free energy of carbon in austenite (\bar{G}_C^Y) is calculated for the austenite in equilibrium with ferrite and cementite. Since the activity of carbon, ahead of the pearlite/austenite interface, in austenite must be uniform, the two values of \bar{G}_C^Y must be equal. With the help of the computer iterations the unique partitioning condition at a given temperature can be calculated. A computer

programme for determining such a condition is given in Appendix (IV).

Fe-C-Ni System: In the case of Fe-C-Ni, steady state pearlite growth in the partitioning region is not feasible according to the growth model discussed above, because Ni segregates into the austenite with respect to both the ferrite and the cementite phases. Figure (8) shows the equilibrium phase boundaries for Fe-C-Ni system. Ni is an austenite stabiliser, therefore, the tie-lines in the $\alpha + \gamma$ and the $\gamma + \text{cm}$ two phase fields have different (opposite) slopes. The construction similar to Figure (7) is not possible in the case of Ni. The growth of pearlite in Fe-C-Ni system, therefore, takes place only by para-equilibrium and/or local-equilibrium no-partition mechanisms.

Fe-C-Si System: The partitioning concentrations for the Fe-C-Si steel are calculated assuming zero solubility of silicon in cementite. Silicon being a ferrite stabiliser goes completely into the ferrite. Therefore, pearlite, in this system, grows by partitioning of the alloying element at all temperatures. The equilibrium concentrations for the ferrite-austenite equilibrium are calculated in a way similar to that for Fe-C-Cr and Fe-C-Mn systems. Figure (9) shows, schematically, the equilibrium phase boundaries for Fe-C-Si. Since all the silicon goes to ferrite in this case and $y_{\text{Fe}}^{\text{cm}}$ and y_{C}^{cm} are known, point c (Figure (9)) representing the concentration of silicon in austenite in equilibrium with

cementite, i.e., Y_M^Y can be calculated using the following mass balance condition

$$Y_{Si}^Y \cdot V^\alpha + Y_{Si}^{cm} \cdot V^{cm} = Y_{Si}^O \quad (III.32)$$

where, V^α and V^{cm} represent the volume fractions of ferrite and cementite and Y_{Si}^O stands for the concentration of silicon in the original alloy. Since Y_{Si}^{cm} is equal to zero, Y_{Si}^Y can be calculated as

$$Y_{Si}^Y = \frac{Y_{Si}^O}{V^\alpha} \quad (III.33)$$

For this value of Y_{Si}^Y the austenite cementite phase boundary is calculated. Now assuming a uniform carbon activity in austenite ahead of the austenite/pearlite interface, point c can be determined from the intersection of the carbon iso-activity line, drawn from the austenite end of the tie-line defining ferrite-cementite equilibrium, and the phase boundary defining austenite and the (austenite + cementite) equilibrium. The driving force for silicon for the phase boundary diffusion controlled reaction would then be given by $C_M^{Y^{cm}} - C_M^{Y^\alpha}$. Computer programme for the determination of the partitioning condition for Fe-C-Si is given in Appendix (V).

III.3.b High Supersaturation Region:

In the high supersaturation region pearlite growth may occur either by para-equilibrium or by local-equilibrium no-partition mechanism. The reaction in these cases is

controlled by the diffusion of carbon through the bulk austenite. For binary Fe-C system, pearlite growth rate based on the theory developed by Hillert (14,40) is given by

$$v = K \frac{D_C}{S} (C_C^{\gamma\alpha} - C_C^{\gamma cm}) \quad \text{cm/sec} \quad (\text{III.34})$$

where, $C_C^{\gamma\alpha}$ and $C_C^{\gamma cm}$ are expressed in weight percent and the units of D_C is cm^2/sec . Hillert (14) evaluated the value of constant K and found equal to 1.27. With this value of K the calculated growth rates of pearlite, in Fe-C, were different than the experimental growth rates. In the case of Fe-C-X, the growth of pearlite under para-equilibrium and local-equilibrium no-partition conditions occur in a pseudo-binary manner similar to that in the Fe-C system with the modified phase boundaries. Since the relative effects of alloying elements are of interest in the present work, the value of constant K was recalculated so that the theoretically calculated growth rates match well with the experimental values. The value of the constant K was calculated using the experimental growth rate data given by Brown and Ridley (19) for 0.81% C alloy.

The empirical co-relation for the diffusion coefficient of carbon in austenite given by Kaufmann et al. (41) has been used in the present work. The diffusivity is given by the following expression

$$D_C = D_0 \exp \left(-\frac{Q}{RT} \right) \quad \text{cm}^2/\text{sec} \quad (\text{III.35a})$$

where

$$D_0 = 0.5 \exp(-30 X_C) \text{ cm}^2/\text{sec} \quad (\text{III.35b})$$

and

$$Q = 160,250 - 7.95 \times 10^5 (X_C) + 2.3 \times 10^6 (X_C)^2 \text{ J/mole} \quad (\text{III.35c})$$

where, X_C is the carbon concentration in atom fraction. The average value of X_C was obtained by extrapolating the data of Wells et al. (42) to the average carbon content of the interface, which was calculated as

$$X_C = C_C^{\gamma\alpha} \cdot V^\alpha + C_C^{\gamma\text{cm}} \cdot V^{\text{cm}} \quad (\text{III.36})$$

where, V^α and V^{cm} represent the volume fraction of ferrite and cementite, respectively. The calculated values of $C_C^{\gamma\alpha}$ and $C_C^{\gamma\text{cm}}$ were used. The value of the constant, K, obtained was 2.61. The equation used, for the calculation of pearlite growth rate in Fe-C-X systems, in the present work is

$$v = 2.61 \frac{D_C}{S} (C_C^{\gamma\alpha} - C_C^{\gamma\text{cm}}) \quad (\text{III.37})$$

Thus the possible error in the calculated growth rates of pearlite in the Fe-C-X system has been minimised by using the calculated value of K. The calculated and experimental growth rates for 0.81% carbon steel are shown in Figure (10).

CHAPTER IV

RESULTS AND DISCUSSION

The results of the calculated pearlite growth rates under para-equilibrium, local-equilibrium no-partition and partitioning conditions are presented in the present chapter. These theoretically obtained growth rates are compared with the experimentally determined growth rates available in literature.

IV.1 Fe-C-Mn

Two steels containing 0.8% C - 1.08% Mn and 0.69% C - 1.8% Mn have been studied. The calculated para-equilibrium and local-equilibrium no-partition phase boundaries for these alloys are shown in Figure (11) and Figure (12), respectively. The pearlite growth rates under these conditions have been calculated from equation (III.37) using $(C_C^{\gamma\alpha} - C_C^{\gamma\text{cm}})$ values from Figures (11) and (12) and experimentally (45) determined S values. The calculated effective driving force for the partitioning reaction at low supersaturations is plotted in Figure (13) for both the alloys. The growth rate calculated under partitioning condition using the S values determined by Ridley et al. (45) from equation (III.30) is plotted in Figures (14) and (15), respectively, along with the experimentally observed (22,45) para-equilibrium and local-equilibrium no-partition growth rates.

83415

The partitioning of manganese between the ferrite and the cementite phases has been calculated from the equation given by Razik et al. (23)

$$K_{\alpha}^{\text{cm}}(\text{M}) = \frac{(C_{\text{M}}/C_{\text{Fe}})^{\text{cm}}}{(C_{\text{M}}/C_{\text{Fe}})^{\alpha}} \quad (\text{IV.1})$$

where, C_{M} and C_{Fe} are the weight fractions of the alloying element and iron, respectively. The calculated and experimentally determined partitioning coefficients are shown in Figure (16) as a function of temperature.

The calculated A_{e_1} temperatures for the alloys containing 1.08% Mn and 1.8% Mn are 985 K and 971 K, respectively, which are fairly close to the apparent A_{e_1} temperatures 978 K and 961 K, respectively, obtained from the T vs. $\frac{1}{S}$ plot. According to the theory of pearlite growth, discussed earlier, no-partition reaction is expected to occur below local-equilibrium no-partition A_{e_1} . The calculated no-partition temperatures for these alloys are 940 K and 877 K, respectively, which agree reasonably well with the experimentally measured temperatures 944 K and 895 K, respectively (22).

For both the alloys at high temperature and low supersaturations (between equilibrium A_{e_1} and L-E N-P A_{e_1}) the growth rates calculated by partitioning mechanism are consistent with the experimental observations (22,45), whereas, at low temperature high supersaturation range (below L-E N-P A_{e_1}) the calculated growth rates under local-equilibrium

no-partition condition are closer to the experimentally measured growth rates, at relatively higher temperatures and with the decrease in temperature the calculated values under para-equilibrium condition provides a better explanation. As shown in Figure (16), the calculated values of partition coefficient are consistently higher than the experimental values, for both the alloys.

IV.2 Fe-C-Cr

Steels containing 0.82% C - 1.29% Cr and 2.73% C - 1.87% Cr have been studied in the present work. The calculated para-equilibrium and local-equilibrium no-partition phase boundaries are shown in Figures (17) and (18), respectively. Figure (13) shows the calculated driving force for the pearlite reaction at low supersaturations. The growth rates under these conditions are calculated in the same manner as described for Fe-C-Mn. The calculated growth rates under para-equilibrium, local-equilibrium no-partition and partitioning conditions are plotted in Figures (19) and (20) for the 1.29% Cr and 1.87% Cr steels, respectively, along with the experimentally observed values.

The calculated eutectoid temperatures for these steels are 1025 K and 1034 K, respectively, and the apparent A_{e_1} temperatures, obtained from the T vs. $\frac{1}{S}$ plot, are 1016 K and 1034 K, respectively. These values are close enough to suggest that the existing pearlite growth theories are correct. The calculated no-partitioning temperatures

no-partition condition are closer to the experimentally measured growth rates, at relatively higher temperatures and with the decrease in temperature the calculated values under para-equilibrium condition provides a better explanation. As shown in Figure (16), the calculated values of partition coefficient are consistently higher than the experimental values, for both the alloys.

IV.2 Fe-C-Cr

Steels containing 0.82% C - 1.29% Cr and 2.73% C - 1.87% Cr have been studied in the present work. The calculated para-equilibrium and local-equilibrium no-partition phase boundaries are shown in Figures (17) and (18), respectively. Figure (13) shows the calculated driving force for the pearlite reaction at low supersaturations. The growth rates under these conditions are calculated in the same manner as described for Fe-C-Mn. The calculated growth rates under para-equilibrium, local-equilibrium no-partition and partitioning conditions are plotted in Figures (19) and (20) for the 1.29% Cr and 1.87% Cr steels, respectively, along with the experimentally observed values.

The calculated eutectoid temperatures for these steels are 1025 K and 1034 K, respectively, and the apparent Ae_1 temperatures, obtained from the T vs. $\frac{1}{S}$ plot, are 1016 K and 1034 K, respectively. These values are close enough to suggest that the existing pearlite growth theories are correct. The calculated no-partitioning temperatures

for these alloys are 959 K and 934 K, respectively. The experimentally determined no-partition temperature for 1.29% Cr alloy is 964 K, experimental data for the other steel are not available in literature.

For both the alloys the calculated growth rates under partitioning condition in the high temperature low supersaturation range (between equilibrium Ae_1 and L-E N-P Ae_1) seem to agree reasonably well with the experimental observations (22,45). Whereas, at low temperatures (below L-E N-P Ae_1) the local equilibrium no-partition mechanism fits well with the experimentally measured growth rates. The para-equilibrium mechanism shows less satisfactory agreement even at lower temperatures in this range (below L-E N-P Ae_1). The drop in the experimentally observed growth rates at very low temperatures could be the result of strong carbide forming tendency of chromium, which imparts a kind of solute drag effect (14,49) on the pearlite growth.

IV.3 Fe-C-Ni

The alloys containing 0.85% C - 1.98% Ni and 0.77% C - 3.0% Ni have been studied. The pearlite growth in this case is not feasible by the partitioning mechanism, as discussed in Section III.3.a of Chapter III. The calculated para-equilibrium and local-equilibrium no-partition phase boundaries for these alloys are shown in Figures (21) and (22), respectively. Pearlite growth rates under these conditions are calculated in a manner similar to that described

for Fe-C-Mn. The calculated growth rates are plotted against temperature in Figures (23) and (24), respectively, along with the experimentally observed values.

The equilibrium Ae_1 temperatures, calculated by Urhenius (34), for these alloys are 989 K and 980 K, respectively. Apparent Ae_1 temperatures, obtained from the T vs. $\frac{1}{S}$ plot, are 953 K and 929 K, respectively, for the two alloys. The calculated local-equilibrium no-partition temperatures for 1.98% Ni and 3.0% Ni alloys are 949 K and 918 K, respectively, which are closer to the apparent Ae_1 temperatures, obtained from the experimental observations, rather than to the equilibrium Ae_1 . Therefore, it can be concluded that in the case of Fe-C-Ni local-equilibrium no-partition Ae_1 acts as the effective eutectoid temperature below which pearlite reaction is feasible.

For both the alloys the agreement between the calculated growth rates under local-equilibrium no-partition condition and the experimentally observed growth rates is quite reasonable at all temperatures.

IV.4 Fe-C-Si

The alloy containing 0.84% C - 1.99% Si has been studied. As discussed earlier (Section III.3.a) the pearlite reaction in this case is accompanied by the partitioning of alloying element at all temperatures. Therefore, para-equilibrium and local-equilibrium no-partition controlled pearlite growths have no meaning in this case. The calculated

driving force for the phase boundary diffusion of silicon is shown in Figure (13). The calculated growth rates along with the experimental values are plotted in Figure (25). The calculated and apparent Ae_1 temperatures (obtained from T vs. $\frac{1}{S}$ plot) for this alloy are 1062 K and 1038 K, respectively. At all temperatures the calculated and experimental pearlite growth rates are in reasonably good agreement. Calculated growth rates at lower temperatures (below about 985 K) are below the experimentally observed values, this may be attributed to the, most likely, involvement of the carbon diffusion which has not been considered in the present work for the calculation of the growth rate.

CHAPTER VCONCLUSIONS

1. The pearlite growth rates under the para-equilibrium, local-equilibrium no-partition and partitioning conditions have been determined using the calculated driving force values and the experimentally measured inter-lamellar spacing values available in literature.
2. The calculated pearlite growth velocity for the alloys containing Mn, Cr, Ni and Si have been compared with the experimentally observed results, determined by various investigators. The correlation between the calculated and the experimental results is very good.
3. The results of the calculations carried out in this thesis corroborate the theory of pearlite growth proposed by Sharma et al. (28), Sharma (46), Ridley (45) and others.

REFERENCES

1. S. Ban-ya, J.F. Elliott and J. Chipman: Trans. TMS-AIME, 1969, Vol. 245, p. 1199.
2. S. Ban-ya, J.F. Elliott and J. Chipman: Met. Trans., 1970, Vol. 1, p. 1313.
3. R.L. Orr and J. Chipman: Trans. TMS-AIME, 1967, Vol. 239, p. 630.
4. R.F. Mehl and W.C. Hagel: Prcg. in Metal Phys., 1956, Vol. 6, p. 74.
5. R.F. Mehl: Trans. ASM, 1941, Vol. 29, p. 813.
6. M. Hillert: in "Decomposition of Austenite by Diffusional Processes", Eds. V.F. Zackey and H.I. Aaronson, Interscience Publishers, New York, 1962.
7. R.C. Sharma and G.R. Purdy: Met. Trans., 1974, Vol. 5, p. 939.
8. C. Zener: Trans. AIME, 1946, Vol. 167, p. 550.
9. D. Turnbull: Acta Met., 1955, Vol. 3, p. 55.
10. J.W. Chan: Acta Met., 1959, Vol. 7, p. 18.
11. G. Bolze, M.P. Puls and J.S. Kirkaldy: Acta Met., 1972, Vol. 20, p. 73.
12. W.H. Brandt: J. Appl. Phys., 1945, Vol. 167, p. 139.
13. E. Scheil: Z. Metallkunde, 1946, Vol. 37, p. 123.
14. M. Hillert: in "The Mechanism of Phase Transformation in Crystalline Solids", Inst. of Metals, London, 1981, p. 231.
15. J.M. Shapiro and J.S. Kirkaldy: Acta Met., 1968, Vol. 16, p. 579.
16. B. Sundquist: Acta Met., 1968, Vol. 16, p. 1413.
17. M.P. Puls and J.S. Kirkaldy: Met. Trans., 1972, Vol. 3, p. 2777.
18. R.F. Mehl, C. Wells and W. Batz: Trans. AIME, 1950, Vol. 188, p. 553.

19. D. Brown and N. Ridley: J. Iron and Steel Inst., 1969, Vol. 207, p. 1232.
20. F.E. Bowman: Trans. ASM, 1945, Vol. 35, p. 112.
21. M.L. Picklesimer et al.: Trans. AIME, 1960, Vol. 218, p. 473.
22. N.A. Razik et al.: Acta Met., 1974, Vol. 22, p. 1249.
23. N.A. Razik et al.: Met. Trans. A, 1976, Vol. 6A, p. 209.
24. M. Hillert: Jernkont. Ann., 1952, Vol. 136, p. 25.
25. E. Rudberg: Jernkont. Ann., 1952, Vol. 136, p. 91.
26. J.B. Gilmour et al.: Met. Trans., 1972, Vol. 3, p. 1455.
27. R.C. Sharma and J.S. Kirkaldy: Can. Met. Quart., 1973, Vol. 12(4), p. 391.
28. R.C. Sharma, G.R. Purdy and J.S. Kirkaldy: Met. Trans. A, 1979, Vol. 10A, p. 1119.
29. J.S. Kirkaldy: Can. J. Phys., 1958, Vol. 36, p. 907.
30. D.E. Coates: Met. Trans., 1973, Vol. 4, p. 2313.
31. D.E. Coates: Met. Trans., 1972, Vol. 3, p. 1203.
32. G.R. Purdy, D.H. Weichert and J.S. Kirkaldy: Trans. AIME, 1964, Vol. 203, p. 1025.
33. H. Harvig: Jernkont. Ann., 1971, Vol. 155, p. 157.
34. B. Urhénus: "A Compendium of Ternary Iron-base Phase Diagrams Hardenability Concept with Applications of Steel", Eds., D.V. Doane and J.S. Kirkaldy, AIME, 1970, Vol. 28.
35. M. Hillert and L.I. Staffansson: Acta Chem. Scand., 1970, Vol. 24, p. 3618.
36. F.D. Richardson: J. Iron Steel Inst., 1953, Vol. 175, p. 33.
37. M. Hillert, T. Wada and H. Wada: J. Iron Steel Inst., 1967, Vol. 205, p. 539.
38. R.J. Weiss and K.J. Taver: Phys. Rev., 1956, Vol. 120, p. 1490.
39. M. Hillert and M. Weldenstrom: Met. Trans., 1977, Vol. 8A, p.145.

40. M. Hillert: *Jernkont. Ann.*, 1957, Vol. 141, p. 757.
41. L. Kaufman, S.V. Radcliffe and M. Cohen: in "Thermodynamics of the Bainite Reaction", *Decomposition of Austenite by Diffusional Process*, Eds., V.F. Zackey and H.I. Aaronson, Interscience, New York, 1962, p. 313.
42. C. Wells et al.: *Trans. AIME*, 1950, Vol. 188, p. 553.
43. J.S. Kirkaldy: *Can. J. Phys.*, 1964, Vol. 42, p. 1447.
44. J. Fridberg, L.E. Tornbull and M. Hillert: *Jernkont. Ann.*, 1969, Vol. 153, p. 263.
45. N. Ridley et al.: "Chemical Metallurgy of Iron and Steel", *The Iron and Steel Inst.*, London, 1973.
46. R.C. Sharma: Ph.D. Thesis, McMaster Univ., Canada, 1976.
47. J. Chance and N. Ridley: *Met. Trans. A*, 1981, Vol. 12A, p. 1205.
48. H.I. Aaronson et al.: *Trans. AIME*, 1966, Vol. 236, p. 753.
49. R.C. Sharma and G.R. Purdy: *Met. Trans.*, 1973, Vol. 4, p. 2303.
50. R.C. Sharma: Personal communication.

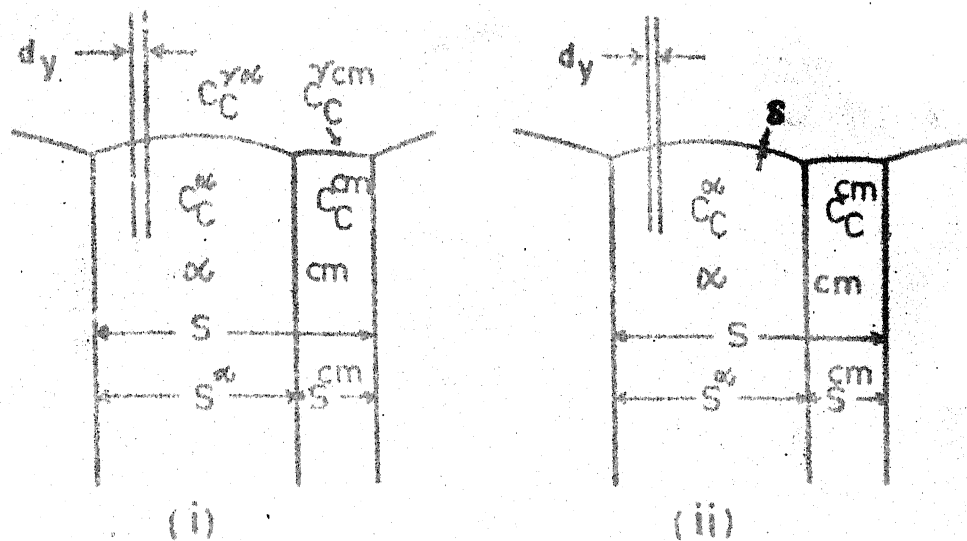


FIG-1. Representation of the growth of lamellar pearlite by (i) volume diffusion and (ii) boundary diffusion.

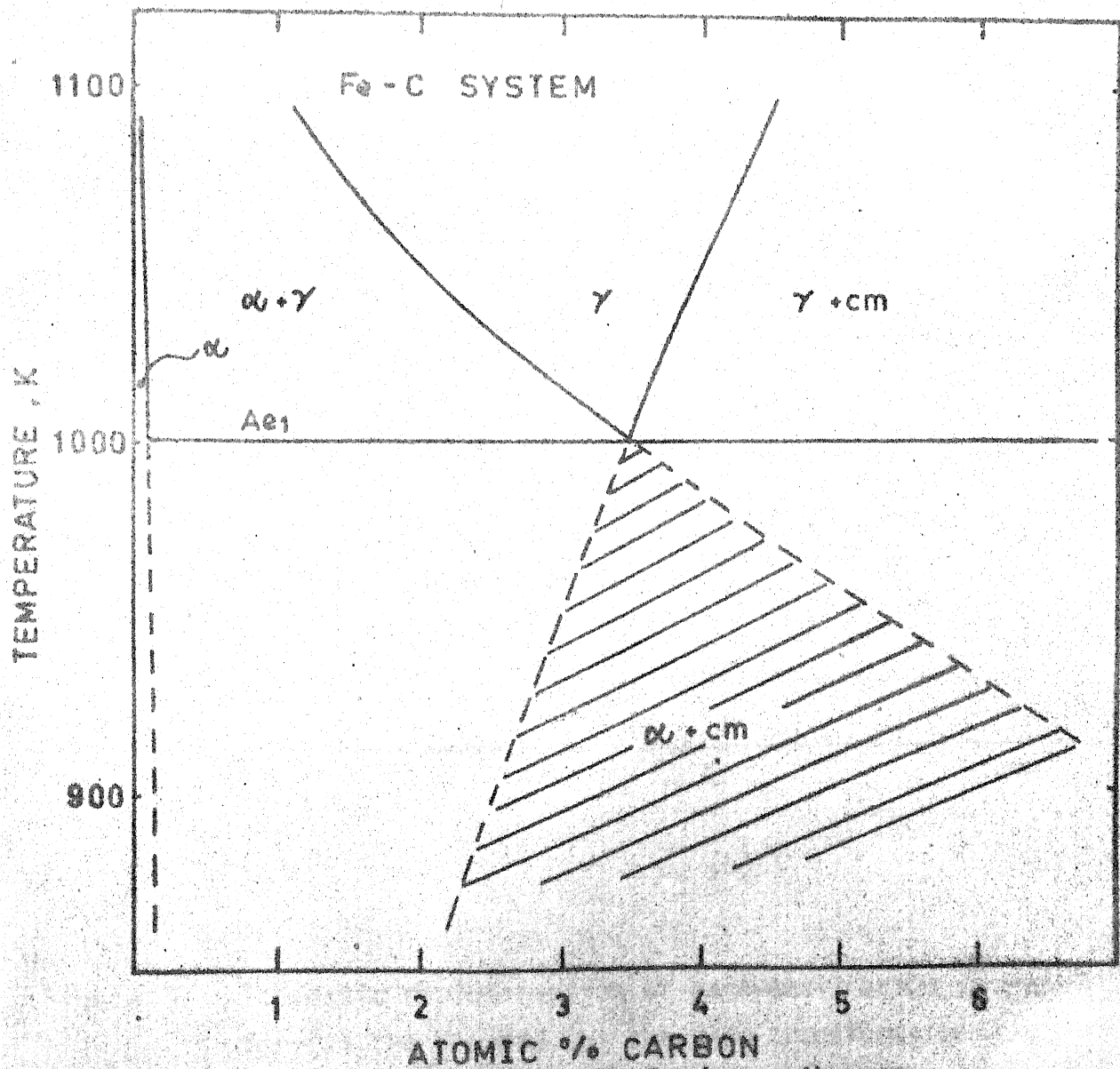
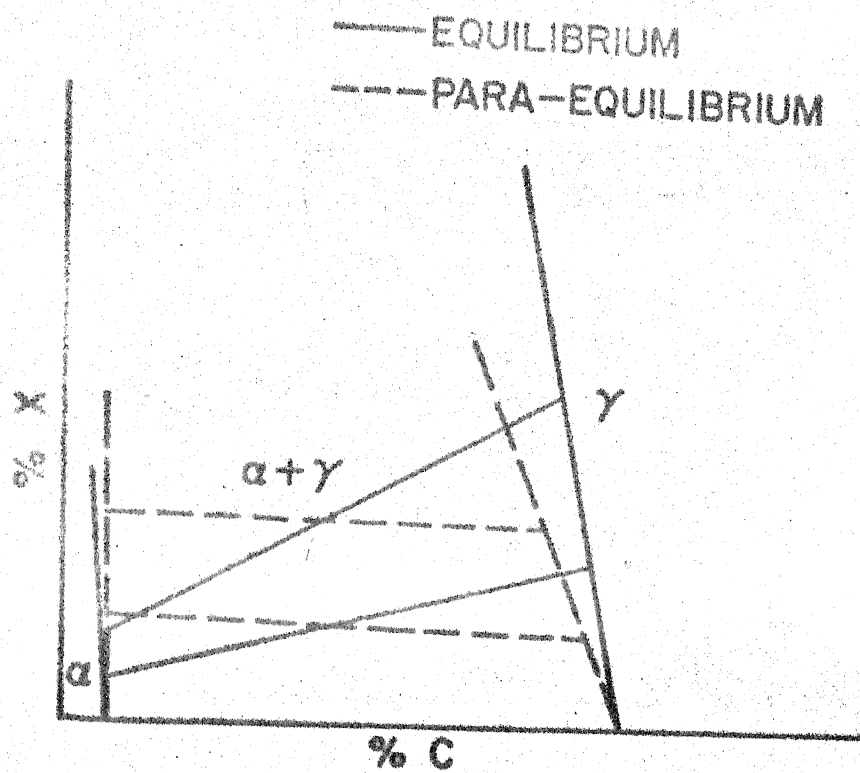
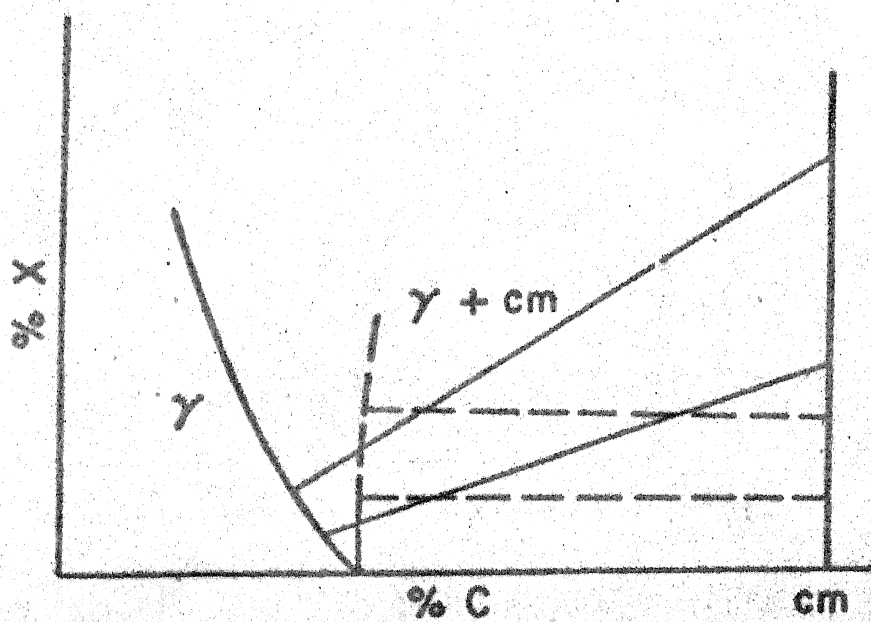


FIG-2. Calculated binary Fe-C phase diagram.

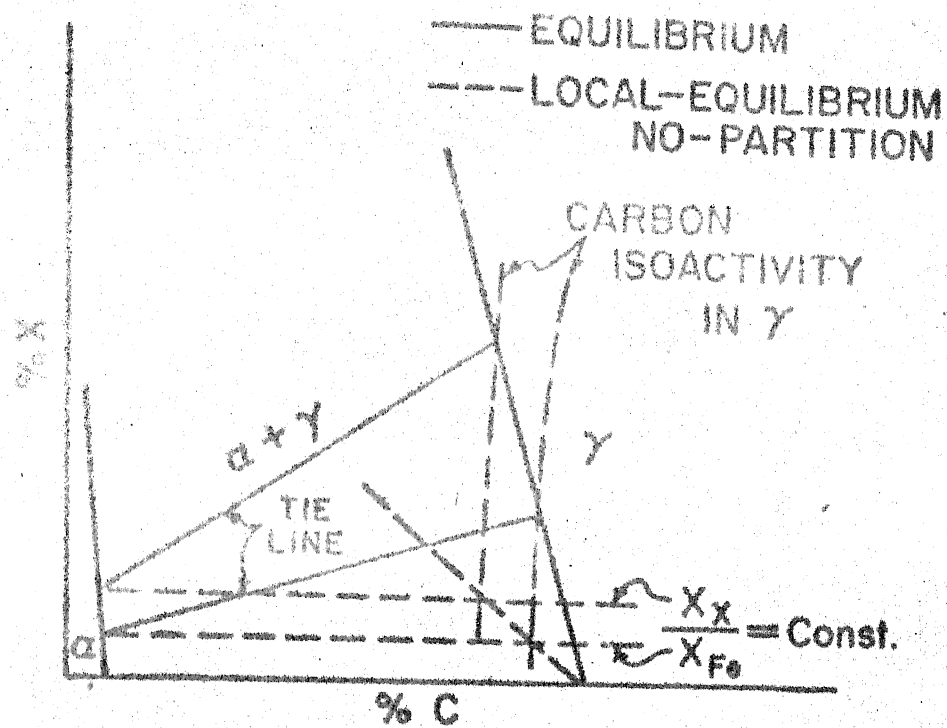


(a)

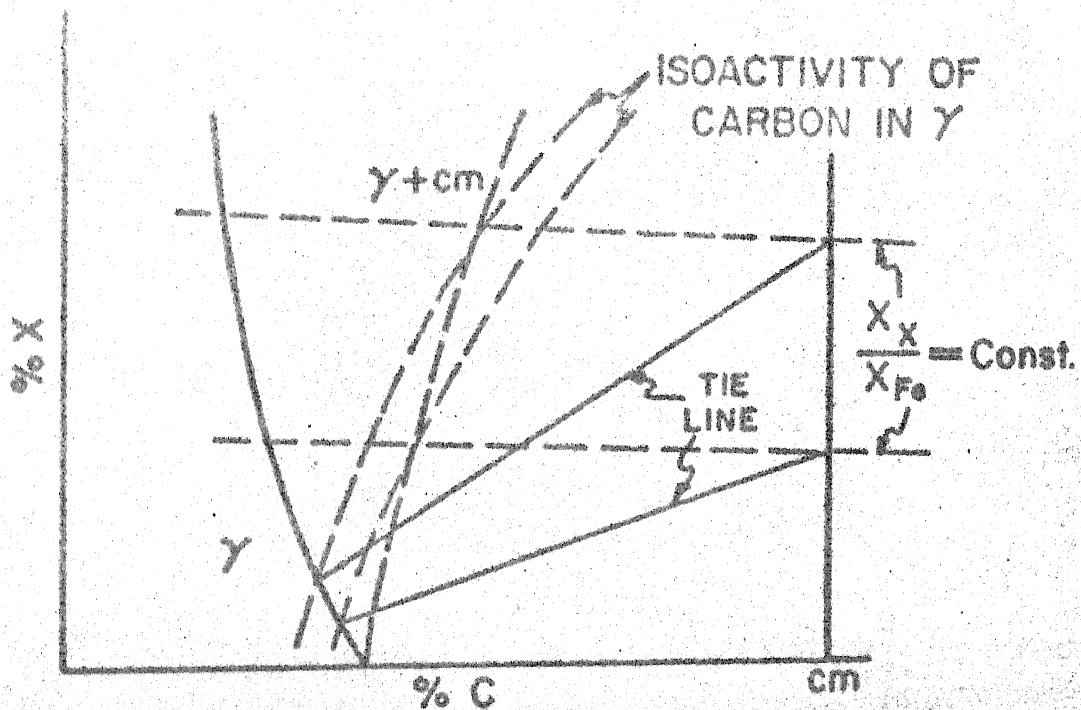


(b)

Figure-3. Schematic representation of para-equilibrium in Fe-C-X system for (a) the $\gamma \rightarrow \alpha$ and (b) the $\gamma \rightarrow cm$ transformation.



(a)



(b)

Figure - 4. Schematic representation of the local equilibrium no-partition phase boundary in the Fe-C-X system for (a) the $\gamma \rightarrow \alpha$ and (b) the $\gamma \rightarrow cm$ transformation.

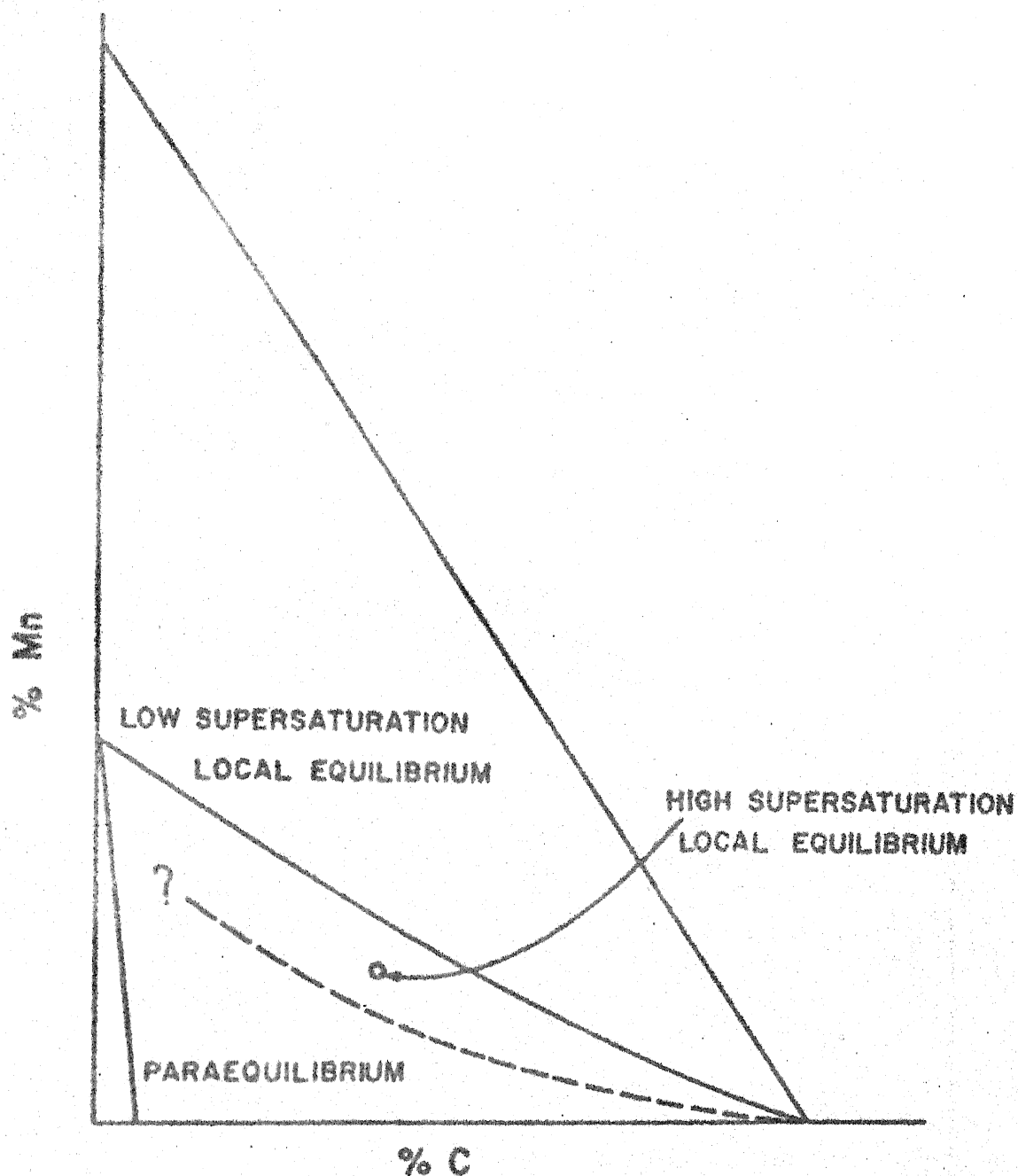
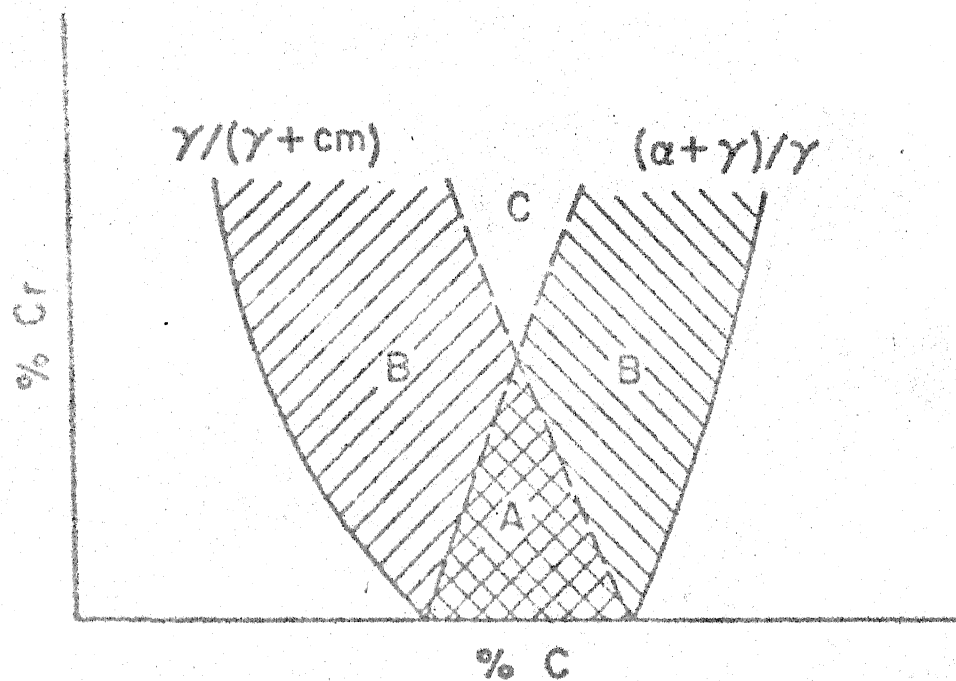
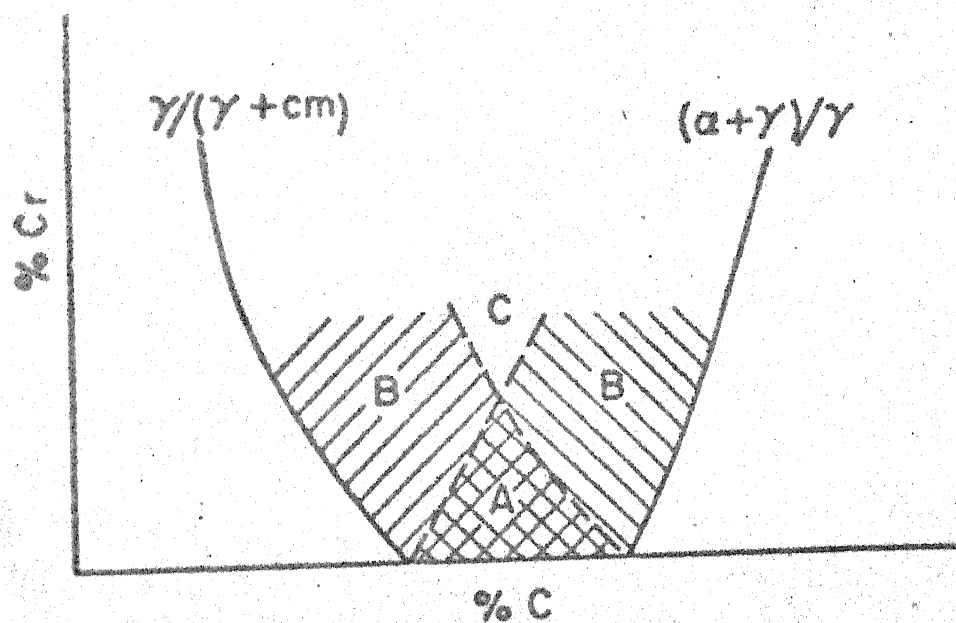


Figure-5. Schematic representation of the local equilibrium - para-equilibrium areas of the proeutectoid transformation in Fe-C-Mn alloys. (after Gilmour)



(a)



(b)

Figure - 6. Schematic partition and no-partition zones in the Fe-C-Cr system in the region of interest for the pearlite transformation (a) para-equilibrium (b) local equilibrium no-partition.

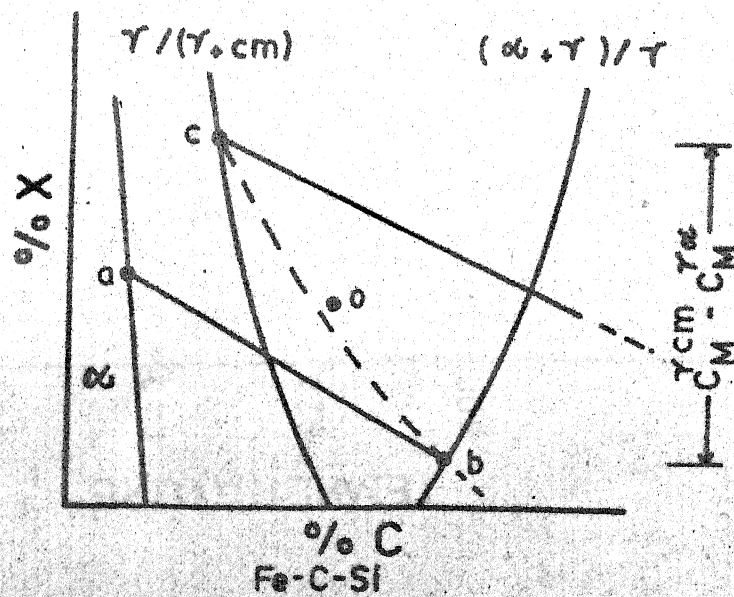
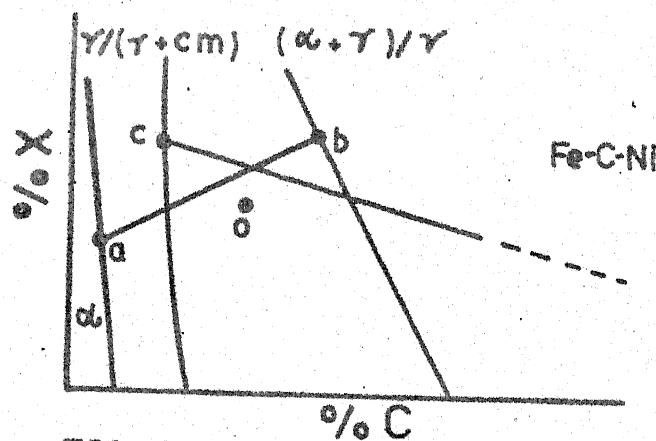
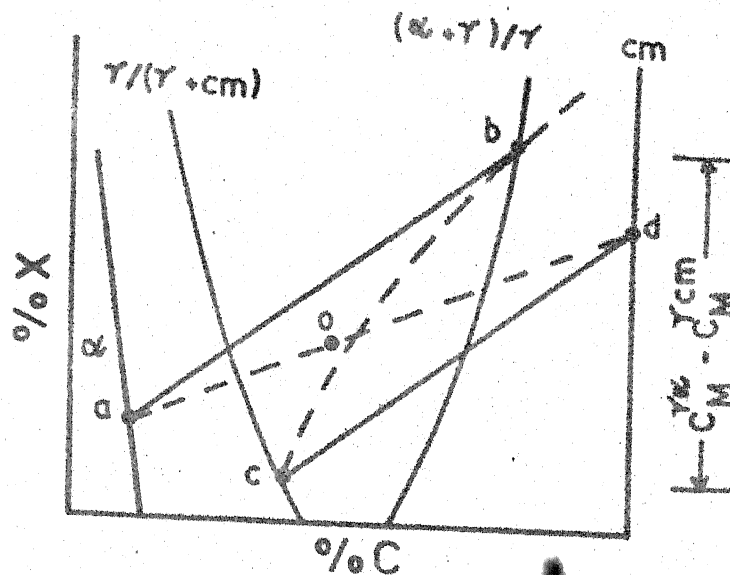


FIG-9
Schematic representation of the partitioning of alloying elements in the low supersaturation range.

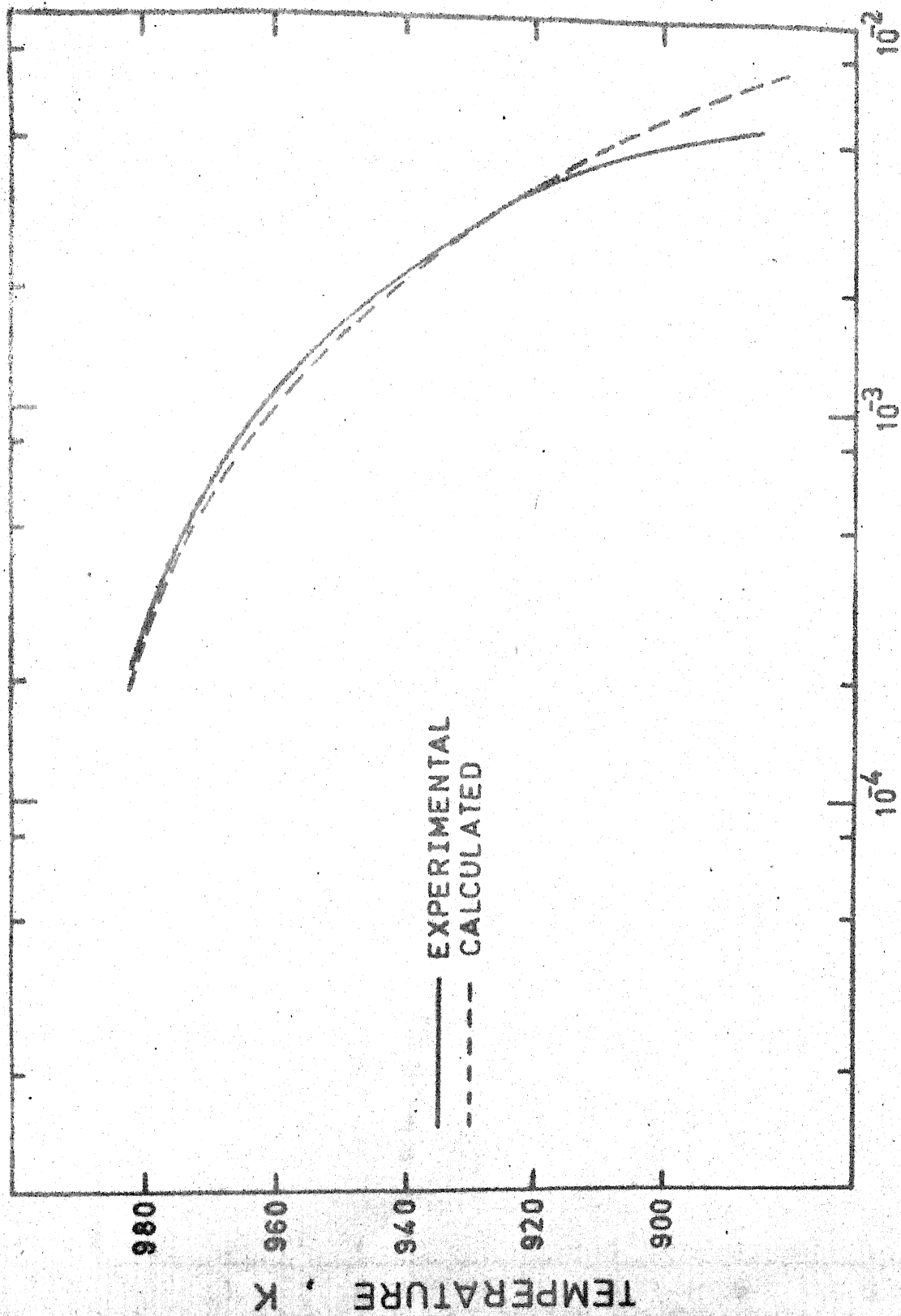


FIG-10. Experimental and calculated growth rates for 0.81% carbon steel.

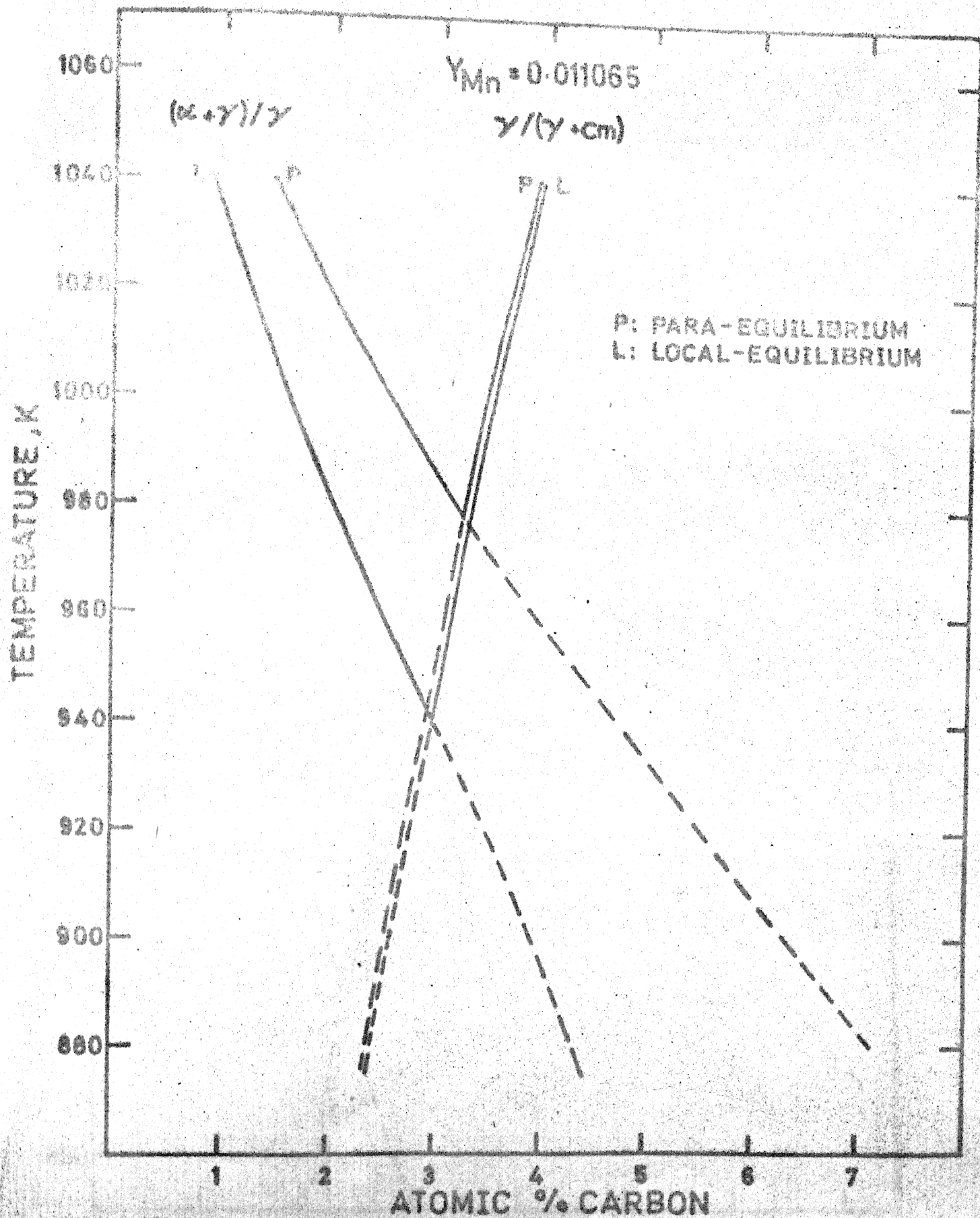


FIG-11. Calculated para-equilibrium and local-equilibrium no-partition phase boundaries for 0.8C-1.08Mn alloy.

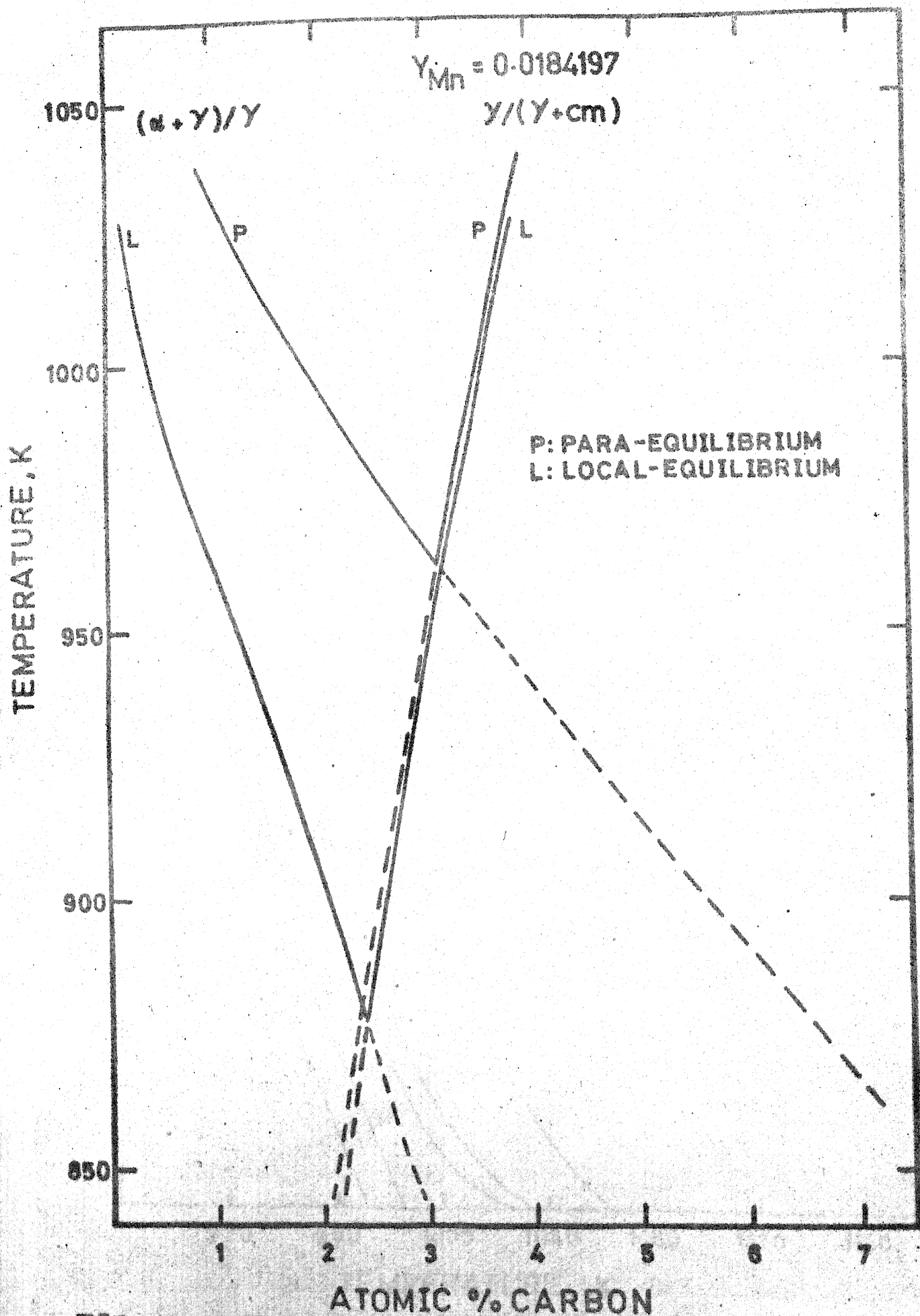


FIG-12. Calculated para-equilibrium and local-equilibrium no-partition phase boundaries for 0.59C-1.8Mn alloy.

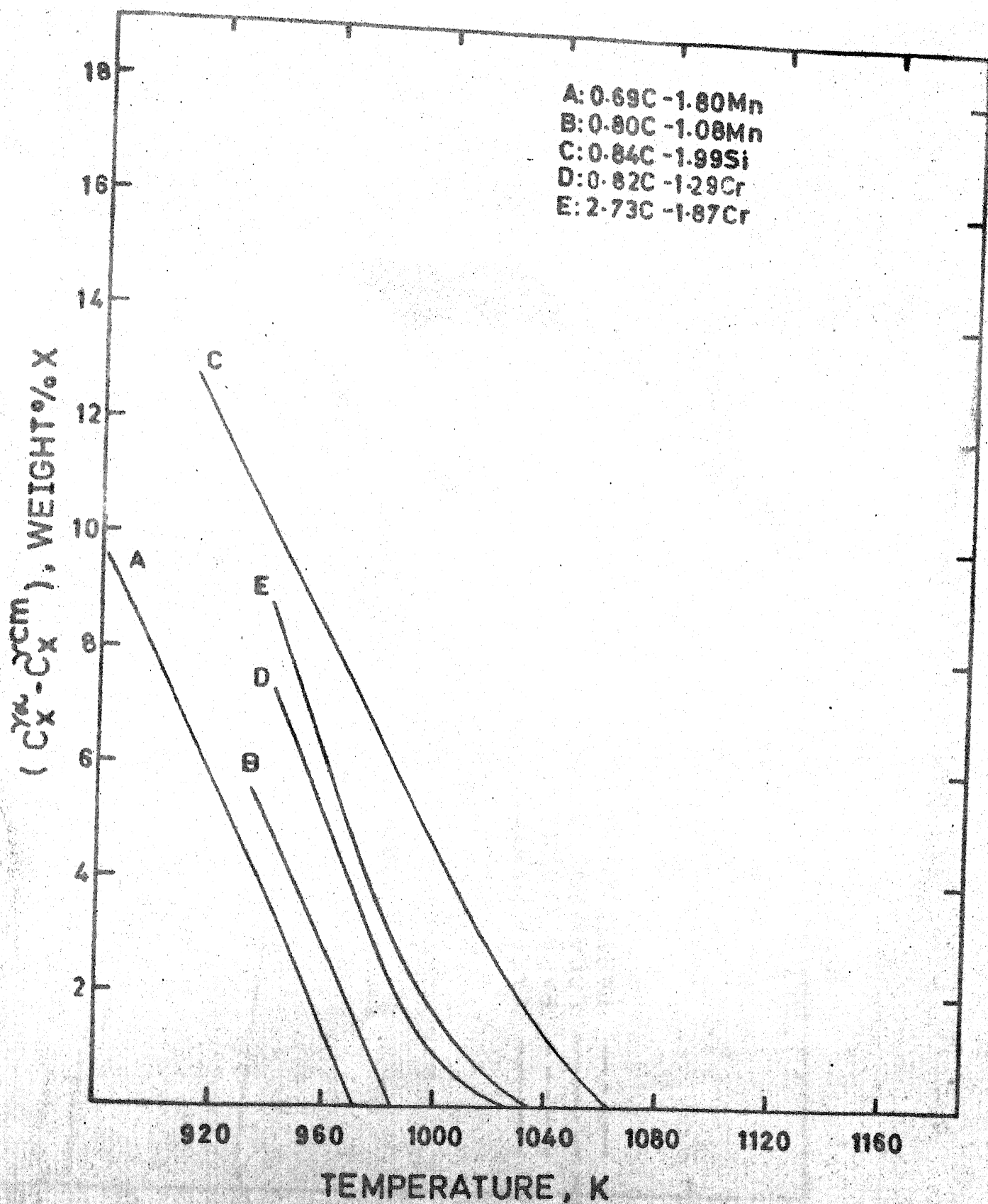
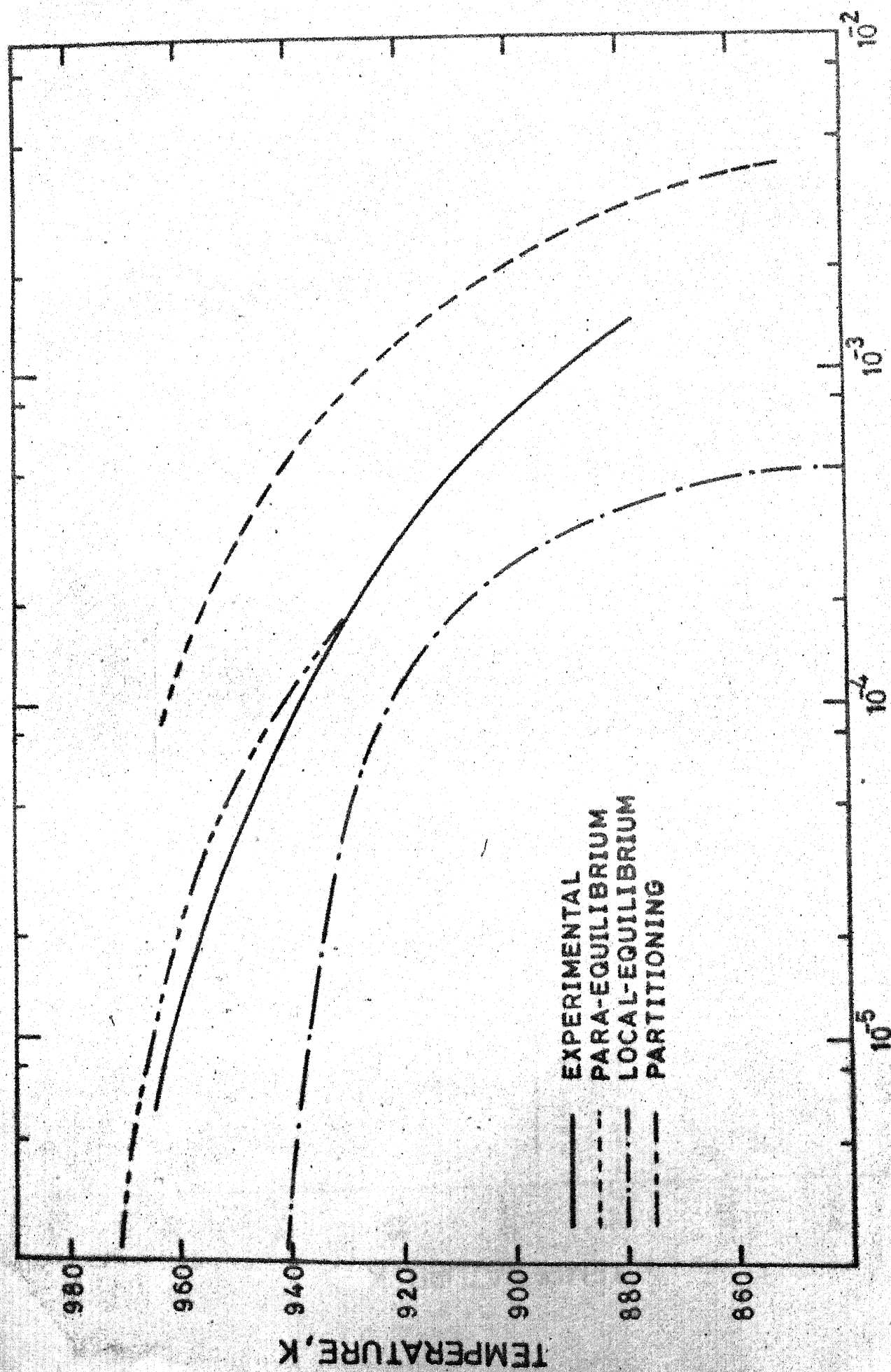


FIG-13. Driving force for phase boundary diffusion at low supersaturations.



GROWTH RATE, CM/S

FIG-14. Calculated and exptl. growth rates for 0.8C-1.08Mn steel.

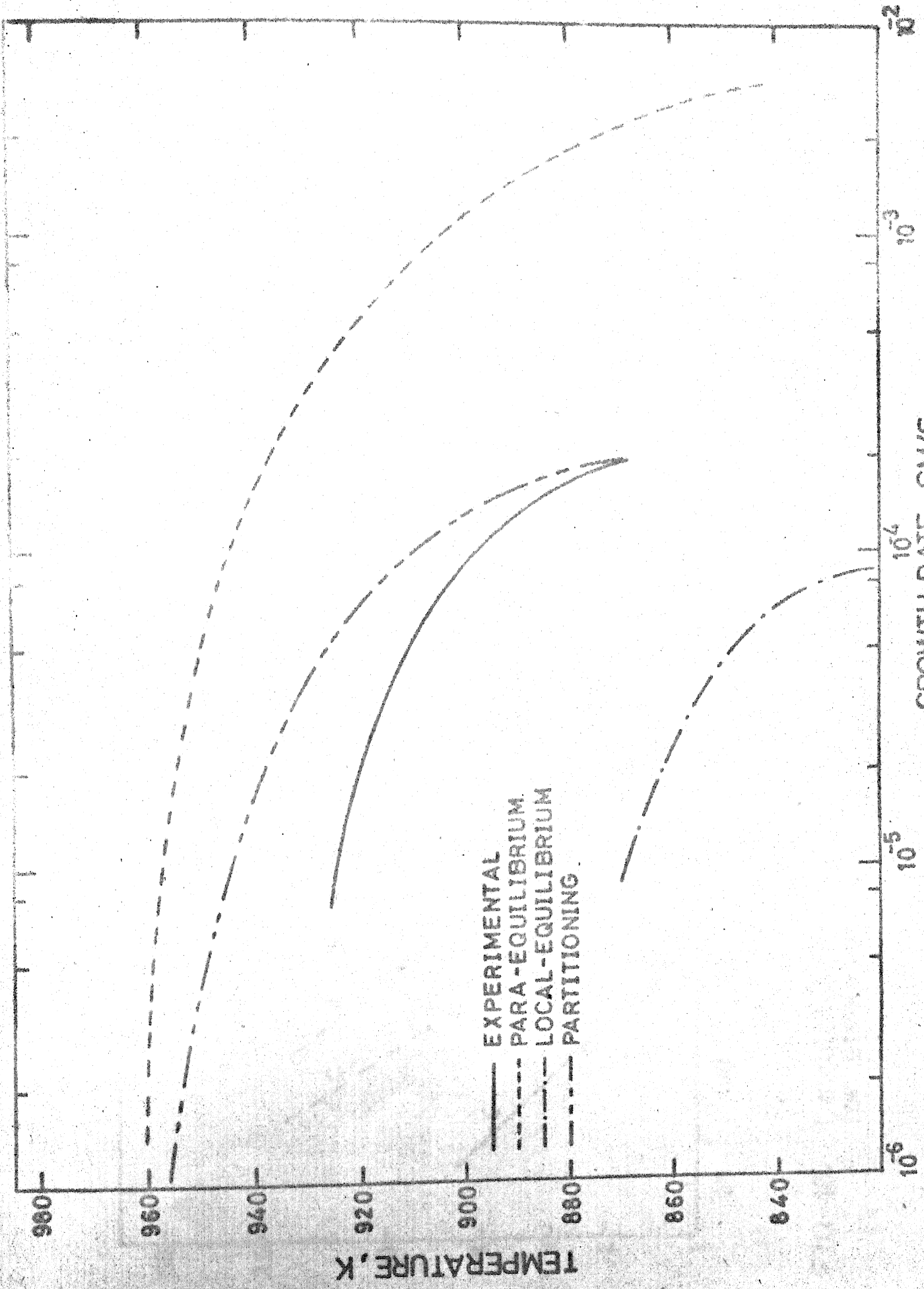


FIG-15. Calculated and experimental growth rates for 0.69C-1.8Mn steel.

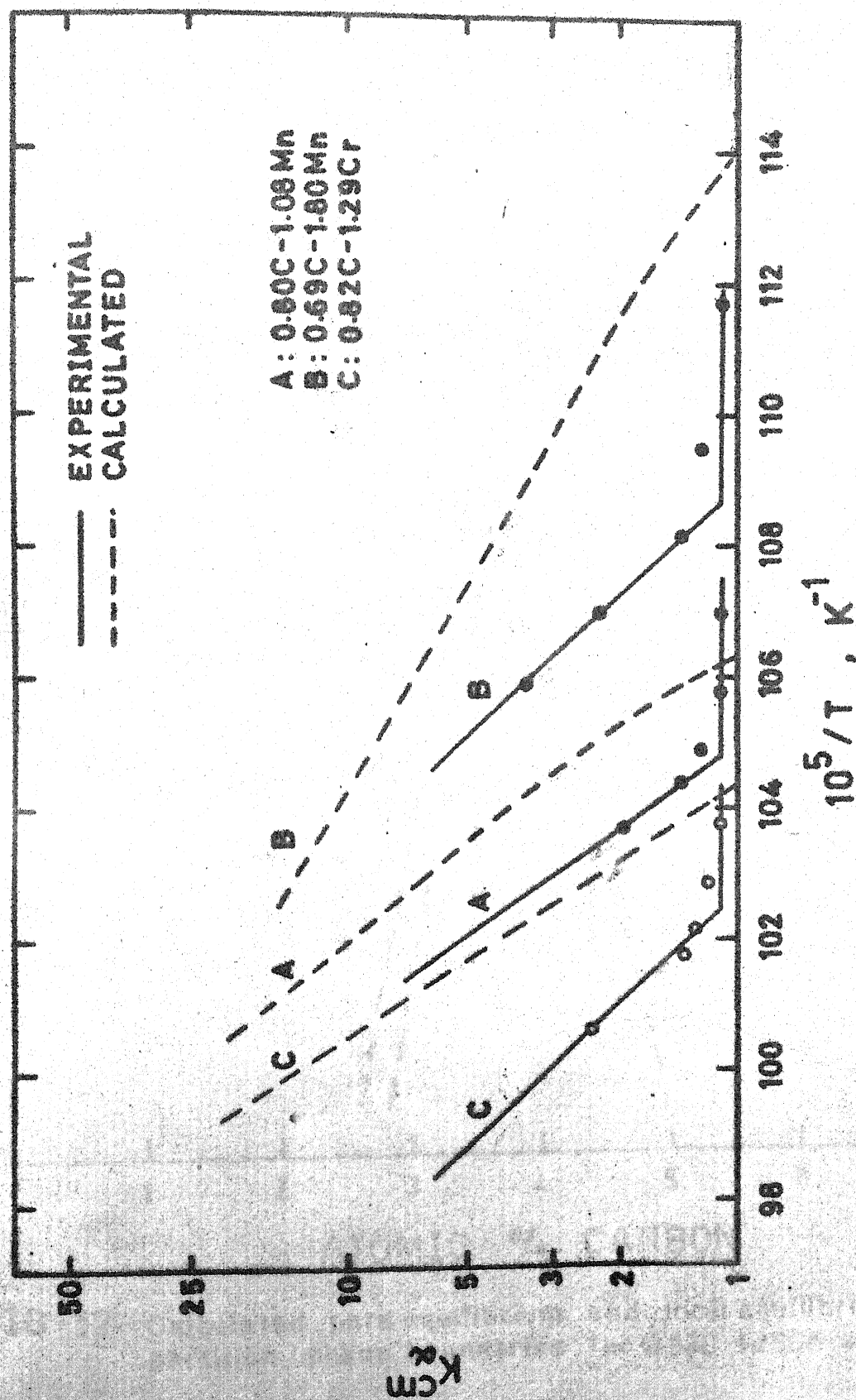


FIG-16. Calculated and experimental(after Razik et al.) partition data for steels at low supersaturations.

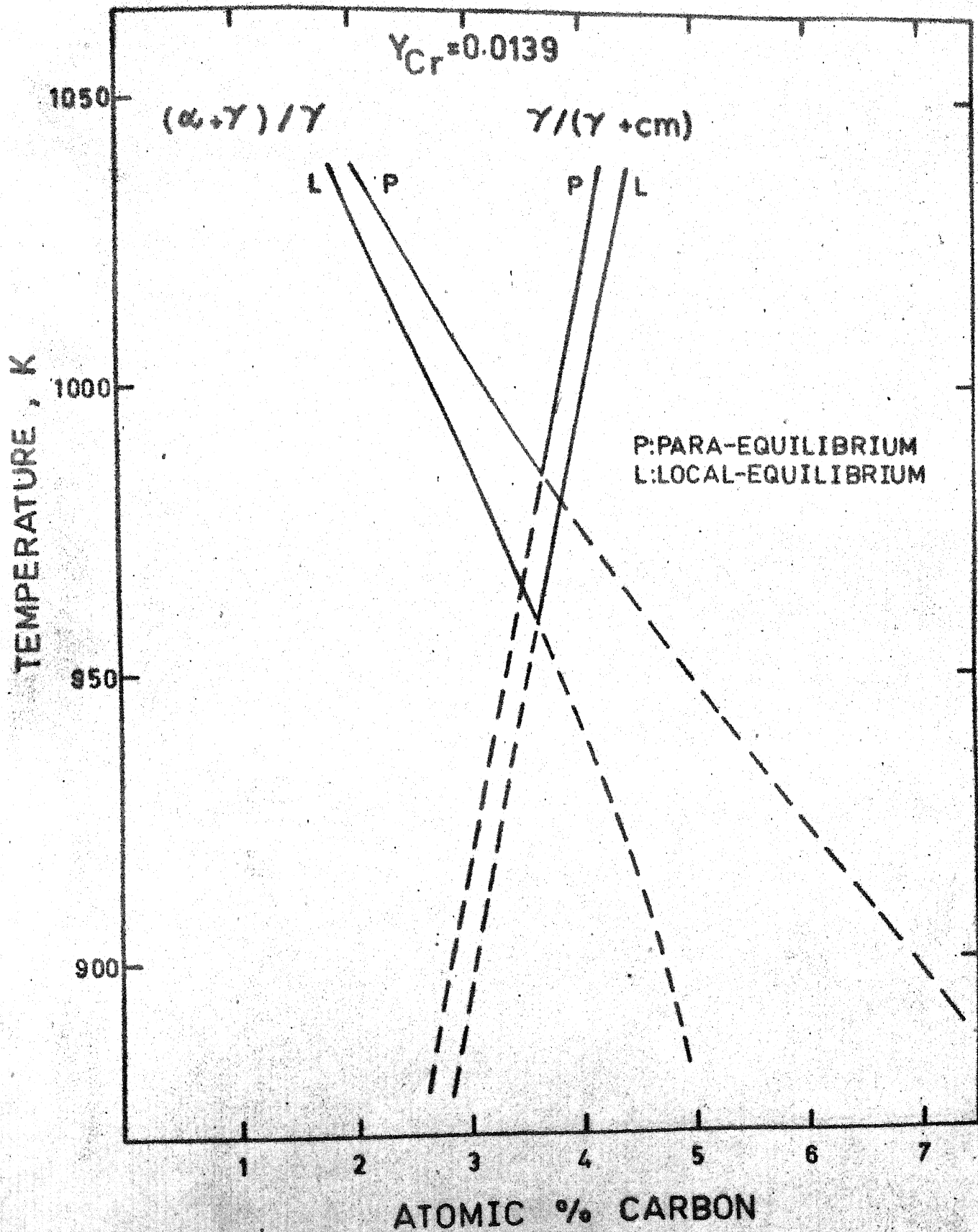


FIG-17. Calculated para equilibrium and local equilibrium no partition phase boundaries for 0.82C-12.9Cr alloy.

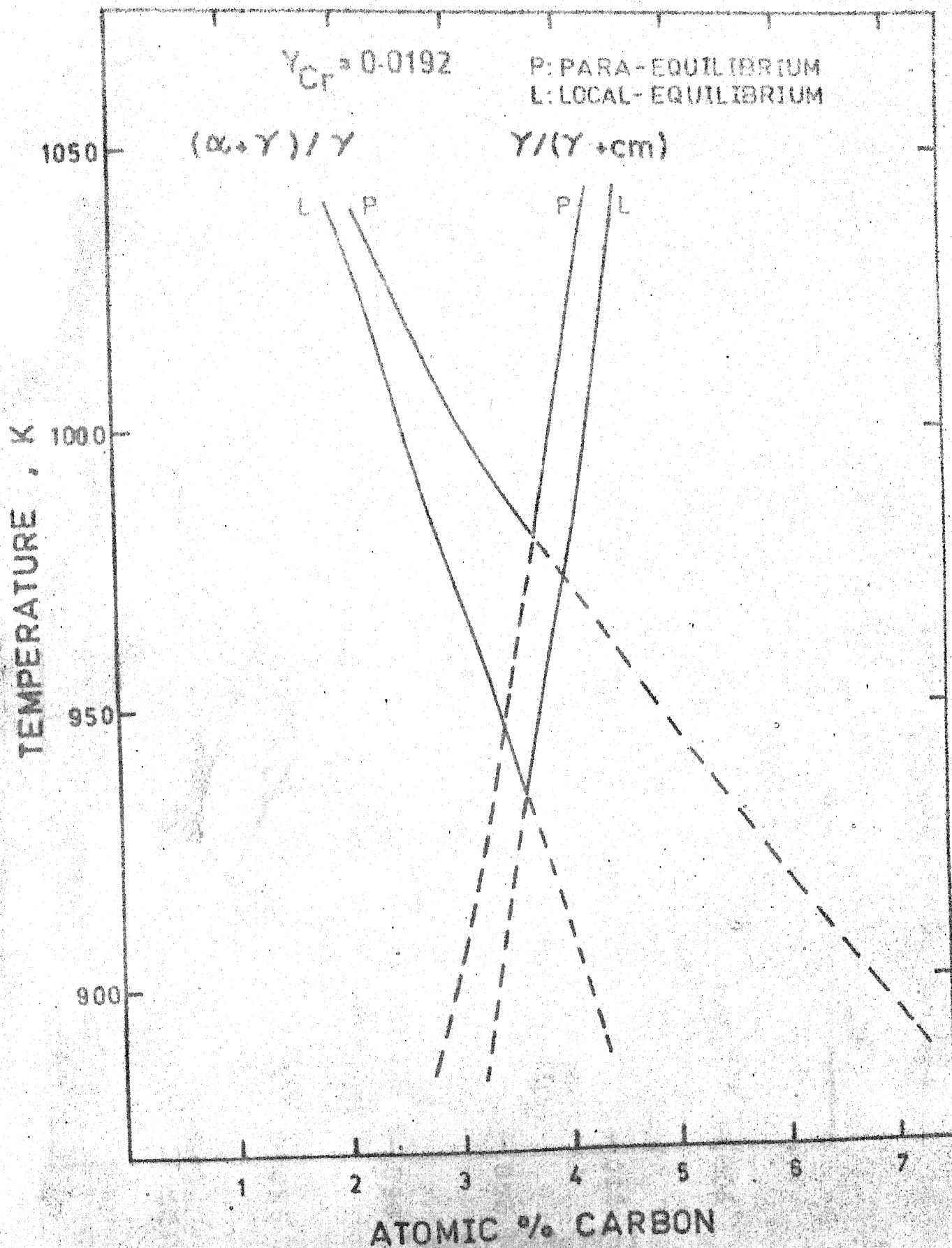


FIG-18. Calculated para-equilibrium and local-equilibrium no-partition phase boundaries for 2.73%C-1.87%Cr alloy.

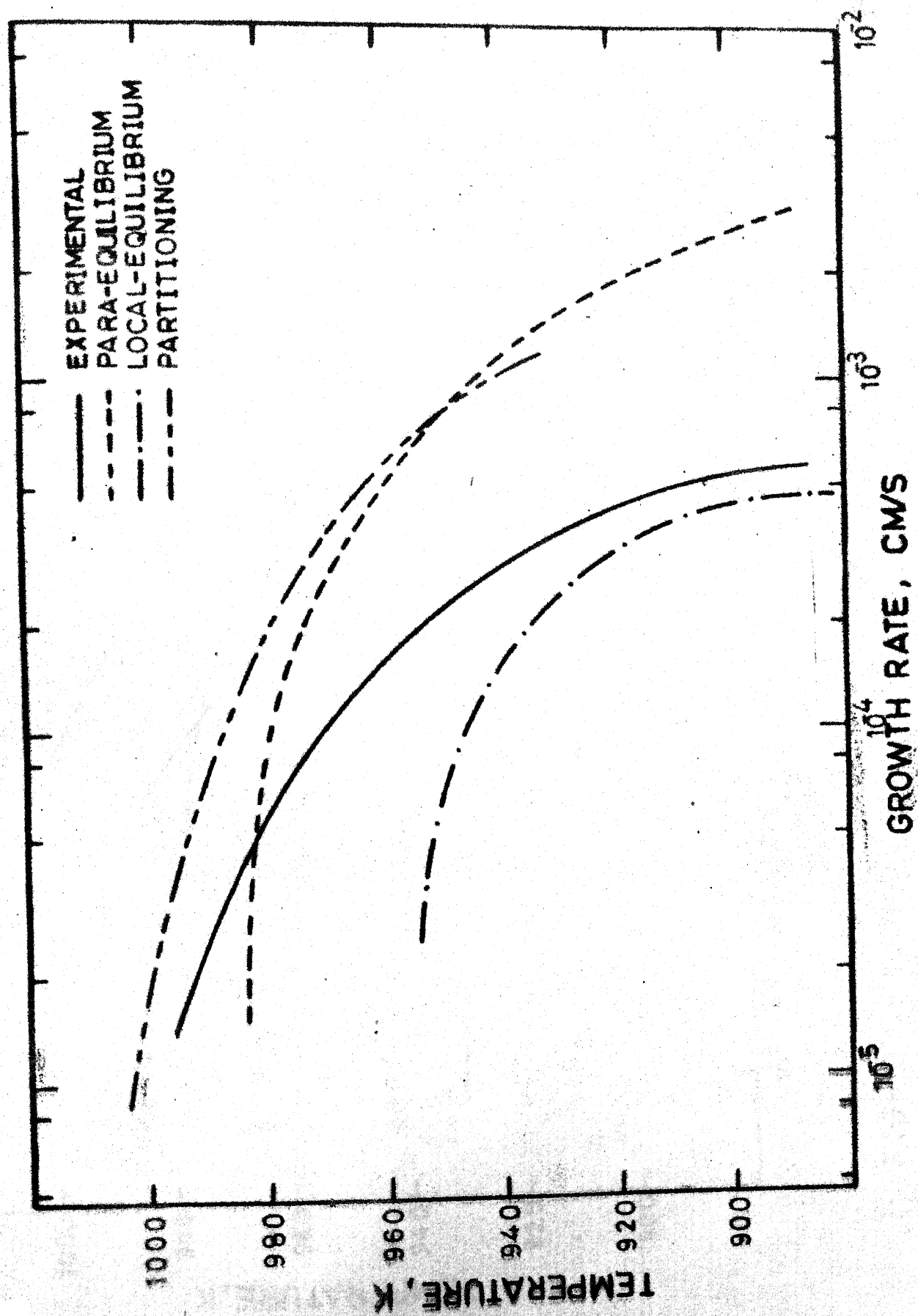


FIG-19. Calculated and exptl growth rates for
0.82C-1.29Cr steel.

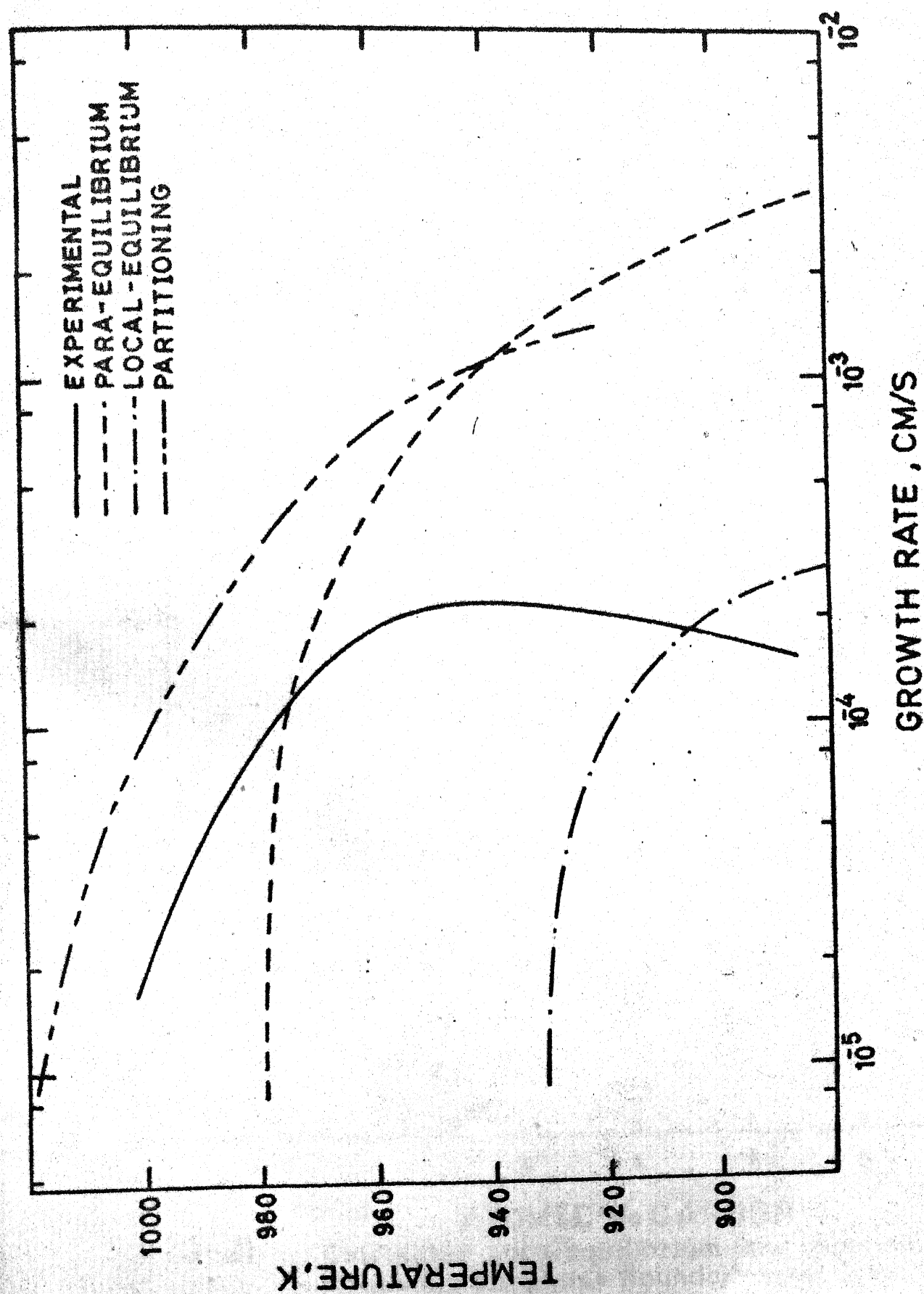


FIG-20. Calculated and Experimental growth rates for 2.73C-187Cr steel.

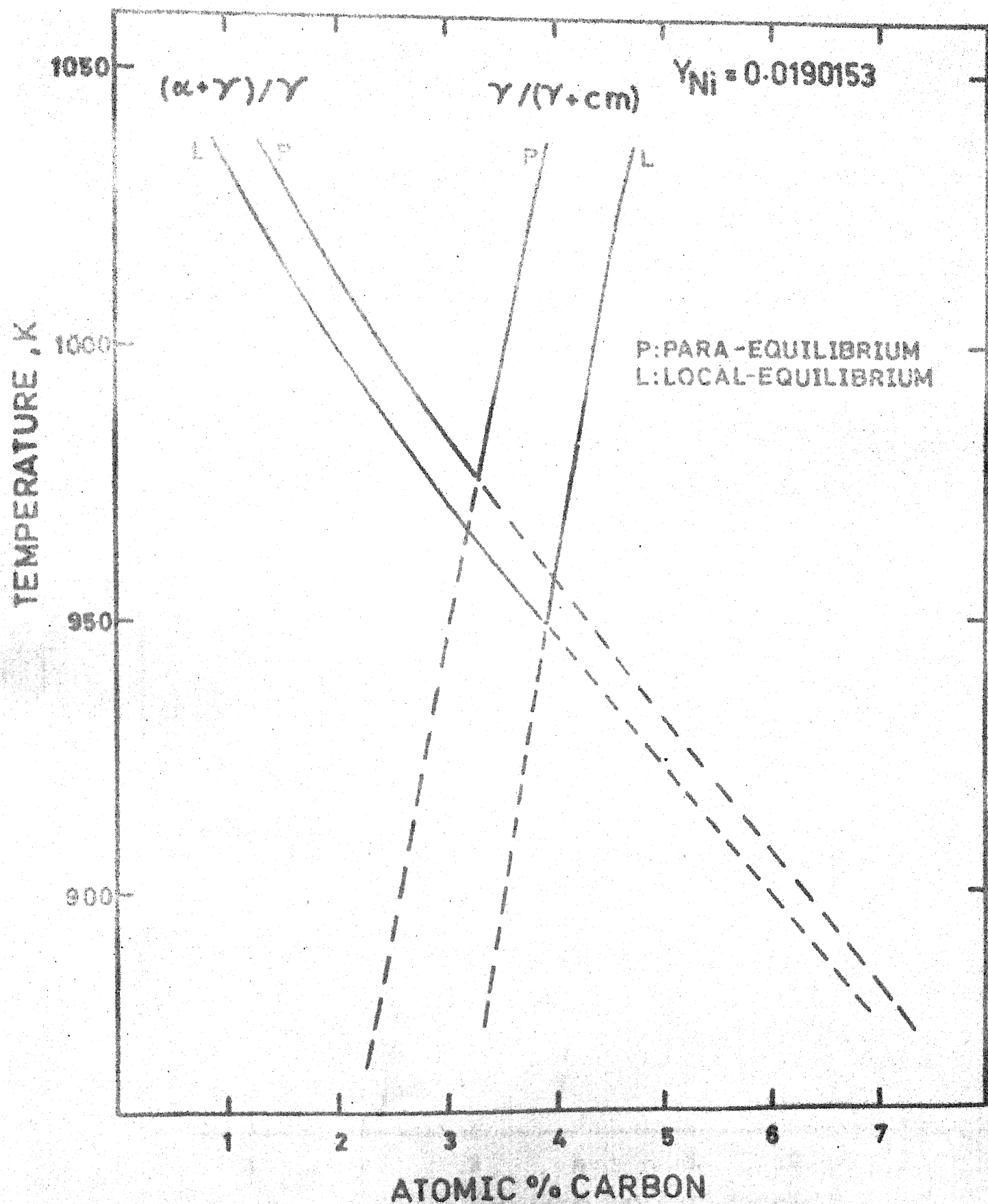


FIG-21.

Calculated para-equilibrium and local-equilibrium no-partition phase boundaries for 0.85C-1.98Ni alloy.

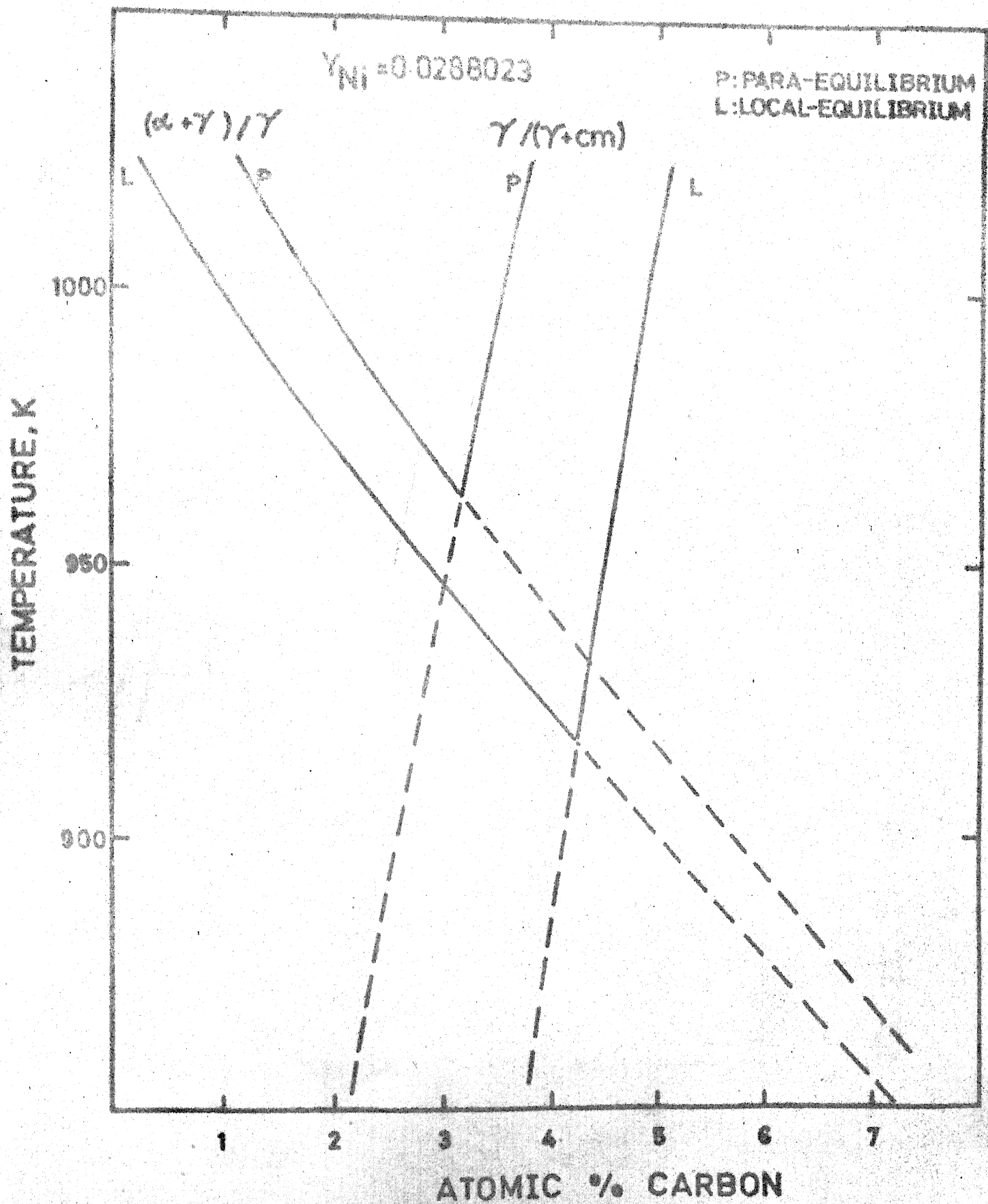


FIG-22. Calculated para-equilibrium and local-equilibrium no-partition phase boundaries for 0.77C-3.0Ni alloy.

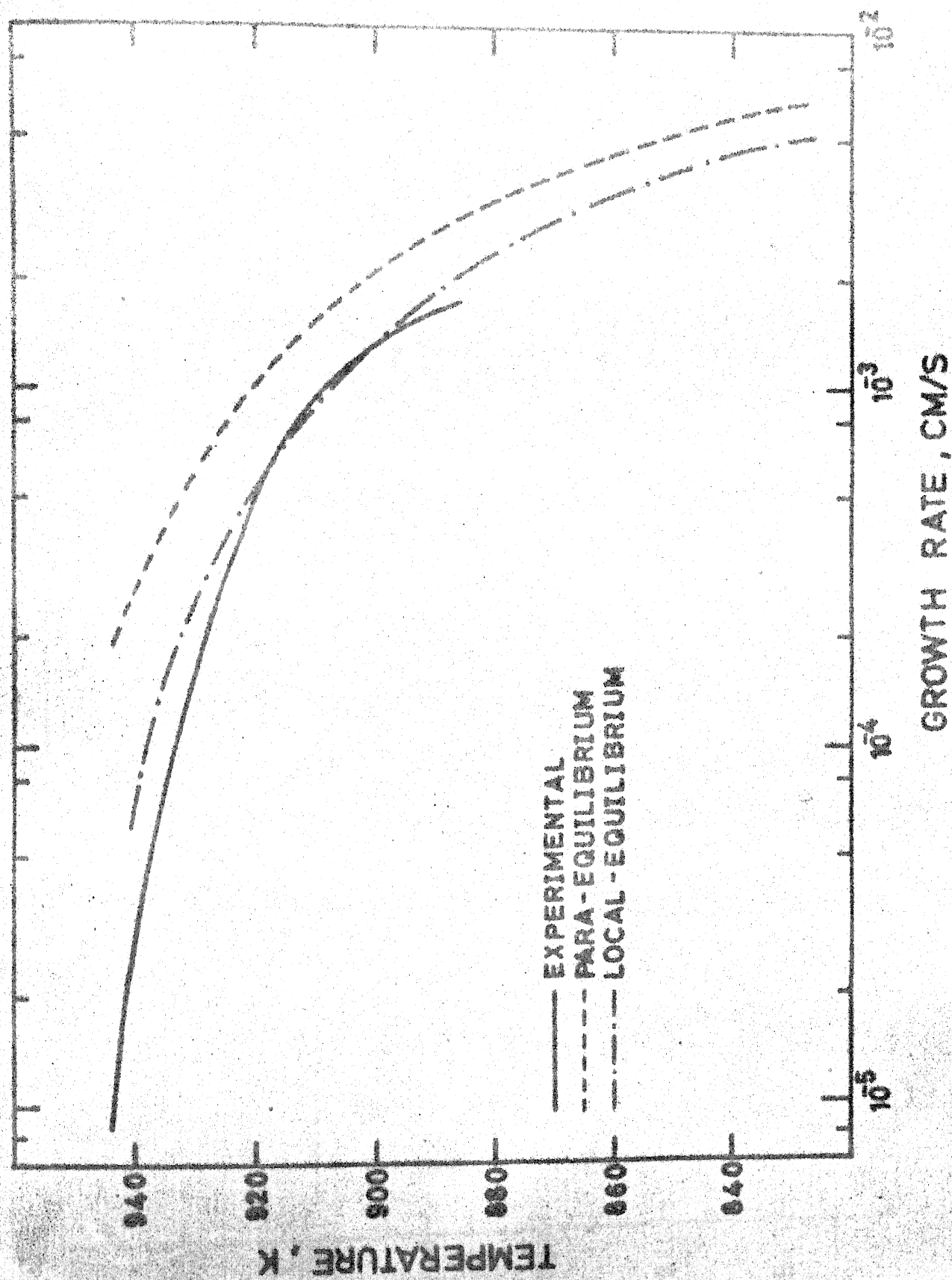
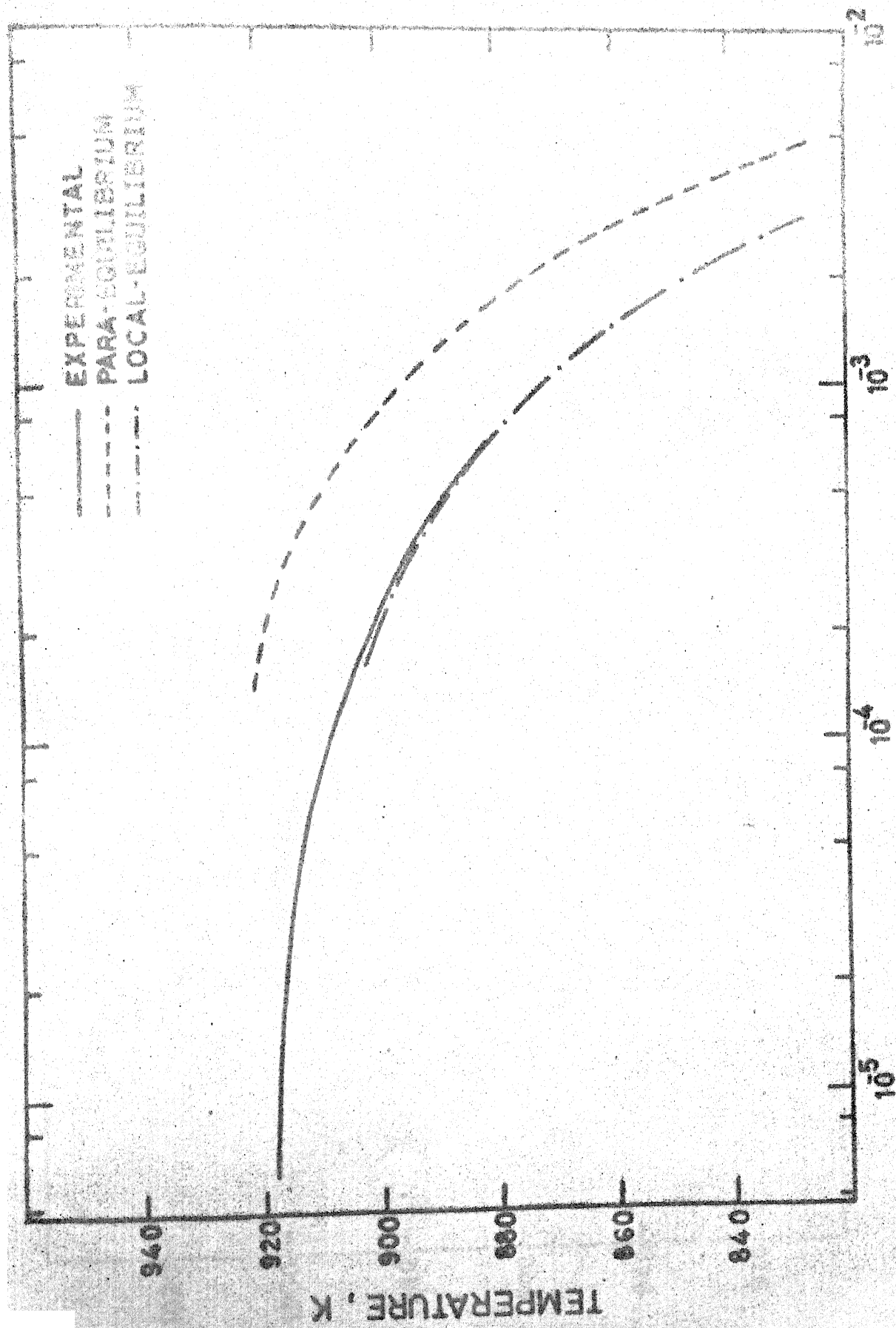
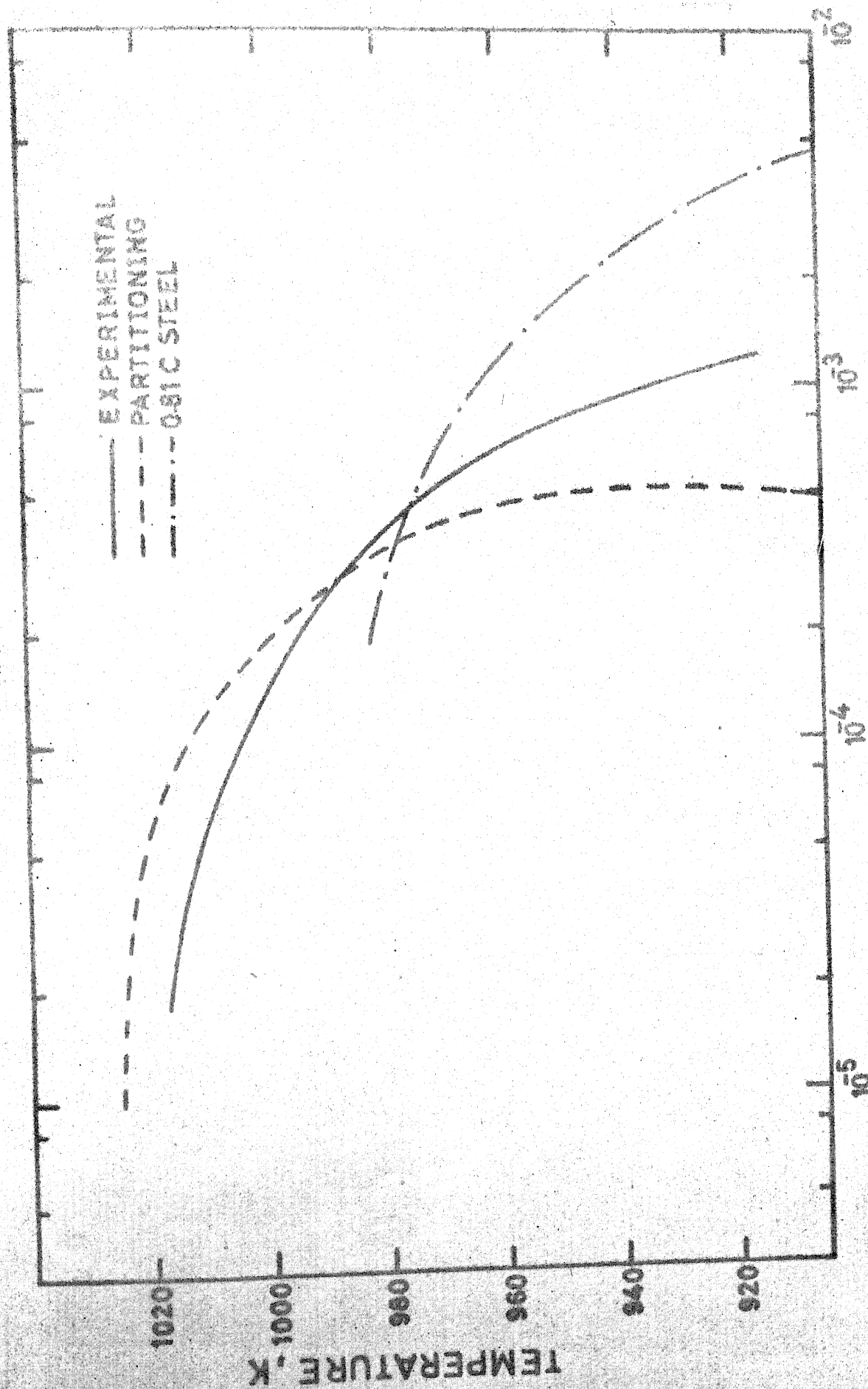


FIG-23. Calculated and Experimental growth rates for 0.05C-1.98Ni steel.



GROWTH RATE , CM/S

FIG-24. Calculated and Experimental growth rates for
077C - 3.0Ni steel.



GROWTH RATE, CM/S

FIG-25. Calculated and Experimental growth rates for 0.81C-1.99Si steel.